

¹
² Susceptible host dynamics explain pathogen resilience to
³ perturbations

⁴
⁵ Sang Woo Park, . . . , Bryan T. Grenfell, Sarah Cobey

⁶ Abstract

⁷ Major priority for epidemiological research in the time of anthropogenic change is un-
⁸ derstanding how infectious disease dynamics respond to perturbations. Interventions
⁹ to slow the spread of SARS-CoV-2 significantly disrupted the transmission of other
¹⁰ human pathogens. As interventions lifted, whether and when respiratory pathogens
¹¹ would eventually return to their pre-pandemic dynamics remains to be answered. We
¹² develop a framework for estimating pathogen resilience based on how fast epidemic
¹³ patterns return to their pre-pandemic, endemic dynamics. Our analysis suggests
¹⁴ that some pathogens may have settled to endemic cycles that are different from their
¹⁵ pre-pandemic patterns. Finally, we show that the replenishment rate of the suscep-
¹⁶ tible pool is a key determinant of pathogen resilience. Our framework offers a novel
¹⁷ perspective to characterizing the dynamics of endemic pathogens and their responses
¹⁸ to SARS-CoV-2 interventions. **[SWP: Need to emphasize broader implications.]**

19 Non-pharmaceutical interventions (NPIs) to slow the spread of SARS-CoV-2 disrupted
 20 the transmission of other human respiratory pathogens, adding uncertainties
 21 to their future epidemic dynamics and the overall public health burden [1]. As
 22 NPIs lifted, large heterogeneities in outbreak dynamics were observed across different
 23 pathogens in different countries, with some pathogens exhibiting earlier resurgences
 24 than others [2, 3, 4]. Heterogeneities in the overall reduction in transmission
 25 and the timing of re-emergence likely reflect differences in NPI patterns, pathogen
 26 characteristics, immigration/importation from other countries, and pre-pandemic
 27 pathogen dynamics [5]. Therefore, comparing the differential impact of the pandemic
 28 NPIs across pathogens can provide unique opportunities to learn about underlying
 29 pathogen characteristics, such as their transmissibility or duration of immunity, from
 30 heterogeneities in re-emergence patterns [6].

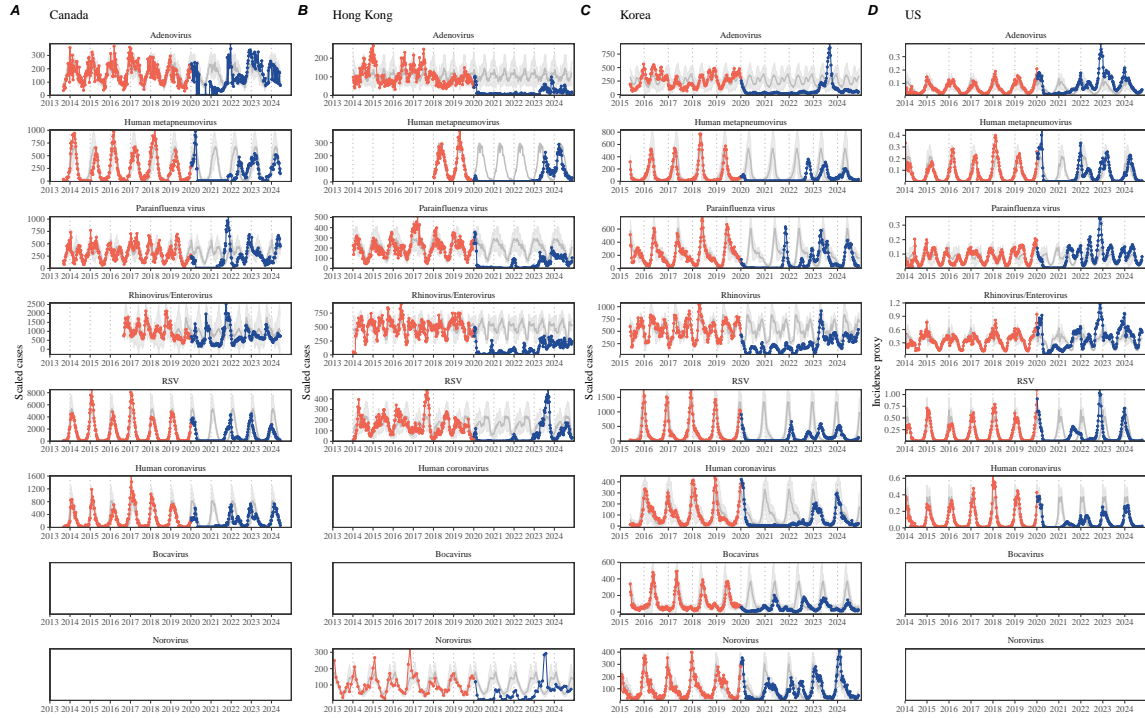


Figure 1: Observed heterogeneity in responses to pandemic NPIs across respiratory pathogens and norovirus in (A) Canada, (B) Hong Kong, (C) Korea, and (D) US. Red points and lines represent data before 2020. Blue points and lines represent data since 2020. Gray lines and shaded regions represent the mean seasonal patterns and corresponding 95% confidence intervals around the mean. Mean seasonal patterns were calculated by aggregating cases before 2020 into 52 weekly bins and taking the average in each week. Cases were scaled to account for changes in testing patterns (Materials and Methods).

31 Even though more than five years have passed since the emergence of SARS-CoV-
 32 2, we still observe persistent changes in pathogen dynamics following the pandemic

33 NPIs: for example, compared to pre-pandemic, seasonal patterns, human metapneu-
34 movirus and bocavirus in Korea are circulating at lower levels, whereas RSV in Korea
35 seem to exhibit different seasonality (Figure 1). These observations suggest a possi-
36 bility for a fundamental change in pathogen dynamics following the pandemic NPIs,
37 which can be driven by permanent shift in either human behavior or population-level
38 immunity [7, 8]. The possibility of a long-lasting impact of the pandemic NPIs pose
39 an important question for future infectious disease dynamics: can we predict whether
40 and when other respiratory pathogens will eventually return to their pre-pandemic
41 dynamics? **[SWP: You suggested: I would say something about the dynamics of**
42 **these pathogens not being well understood, but I've since rewritten the most of intro**
43 **and I'm not sure where I would fit this. If you have any suggestions, let me know...]**

44 So far, the majority of epidemiological analyses of respiratory pathogens in the
45 context of the pandemic NPIs have focused on characterizing the timing of rebound
46 [1, 9, 5]. Instead, we seek to characterize how fast a pathogen returns to its pre-
47 pandemic dynamics. These two concepts have subtle but important differences: for
48 example, it took more than 3 years for human metapneumovirus to rebound in Hong
49 Kong but the observed epidemic patterns in 2024 are similar to pre-pandemic seasonal
50 means, suggesting a rapid return to pre-pandemic dynamics following a perturbation
51 (Figure 1). Measuring this rate of return is particularly useful because it allows us
52 to quantify the ecological resilience of a host-pathogen system [10, 11, 12, 13].

53 In this study, we lay out theoretical and statistical approaches to characterizing
54 the resilience of a host-pathogen system based on how fast the system recovers from
55 perturbation. We begin by laying out a few representative scenarios that capture the
56 potential impact of NPIs on endemic pathogen dynamics and illustrate how resilience
57 can be measured by comparing the pre- and post-pandemic dynamics of susceptible
58 and infected hosts. In practice, information on susceptible hosts is often unavail-
59 able, making this theoretical approach infeasible. Instead, we utilize a mathematical
60 technique to reconstruct empirical attractors from the data [14], which allows us to
61 measure the rate at which the host-pathogen system approaches this empirical attrac-
62 tor after a perturbation; this rate corresponds to the resilience of the host-pathogen
63 system. We use this method to analyze pathogen surveillance data for respiratory
64 and non-respiratory pathogens from Canada, Hong Kong, Korea, and US. Finally,
65 we show that susceptible host dynamics explain variation in pathogen resilience.

66 Conceptual introduction to pathogen resilience

67 In classical ecological literature, resilience of an ecological system is measured by
68 the rate at which the system returns to its reference state following a perturbation
69 [10, 11, 12, 13]. This rate corresponds to the largest real part of the eigenvalues of
70 the linearized system near equilibrium—here, we refer to this value as the *intrinsic*
71 resilience of the system, which represents the expected rate of return from perturbed
72 states. In practice, we rarely know the true model describing population-level dy-

73 namics of common respiratory pathogens, limiting our ability to infer the intrinsic
74 resilience of a system. Instead, we can still measure the *empirical* resilience of a
75 host-pathogen system by looking at how fast the system returns to the pre-pandemic,
76 endemic dynamics after interventions are lifted.

77 As an example, we begin with a simple Susceptible-Infected-Recovered-Susceptible
78 (SIRS) model with seasonally forced transmission and demography (i.e., birth and
79 death). The SIRS model is the simplest model that allows for waning of immunity
80 and is commonly used for modeling the dynamics of respiratory pathogens [15]. First,
81 consider an intervention that reduce transmission by 50% for 6 months starting in
82 2020, which causes epidemic patterns to deviate from its original stable annual cycle
83 for a short period of time and eventually come back (Figure 2A). To measure the
84 resilience of this system empirically, we first need to be able to measure the distance
85 from its pre-pandemic attractor. There are many ways we can measure the distance
86 from attractor, but for illustrative purposes, we choose one of the most parsimonious
87 approach: that is, we look at how the susceptible (S) and infected (I) populations
88 change over time and measure the distance on the SI phase plane (Figure 2B). In this
89 simple case, the locally estimated scatterplot smoothing (LOESS) fit indicates that
90 the distance from attractor decreases exponentially (linearly on a log scale) on aver-
91 age (Figure 2C). Furthermore, the overall rate of return approximates the intrinsic
92 resilience of the seasonally unforced system (Figure 2C).

93 Alternatively, NPIs can have a lasting impact on the pathogen dynamics; as an
94 example, we consider a scenario in which a 10% reduction in transmission persists
95 even after the NPIs are lifted (Figure 2D–F). In such cases in practice, we can-
96 not know whether the pathogen will return to its original cycle or a different cycle
97 until many years have passed, and we cannot measure the distance to the new un-
98 known attractor that the system might eventually approach. Nonetheless, we can
99 still measure the distance from the pre-pandemic attractor and ask how the distance
100 changes over time (Figure 2E). The LOESS fit suggests that the distance from the
101 pre-pandemic attractor will initially decrease exponentially on average (equivalently,
102 linearly on a log scale) and eventually plateau (Figure 2F). Here, a permanent 10%
103 reduction in transmission rate slows the system, which causes the distance from the
104 pre-pandemic attractor initially to decrease at a slower rate (Figure 2F) than it would
105 have otherwise (Figure 2C) before plateauing at a fixed distance between the two
106 attractors. This example shows that resilience is not necessarily an intrinsic prop-
107 erty of a specific pathogen. Instead, pathogen resilience is a property of a specific
108 attractor that a host-pathogen system approaches, which depends on both pathogen
109 and host characteristics.

110 Finally, transient phenomena can further complicate the picture (Figure 2G–I).
111 For example, a stage-structured model initially exhibits a stable annual cycle, but
112 perturbations from a 10% reduction in transmission for 6 months cause the epidemic
113 to shift to biennial cycles (Figure 2G). The system eventually approaches the original
114 pre-pandemic attractor (Figure 2H), suggesting that this biennial cycle is a transient
115 phenomenon. The LOESS fit indicates that the distance from the attractor initially

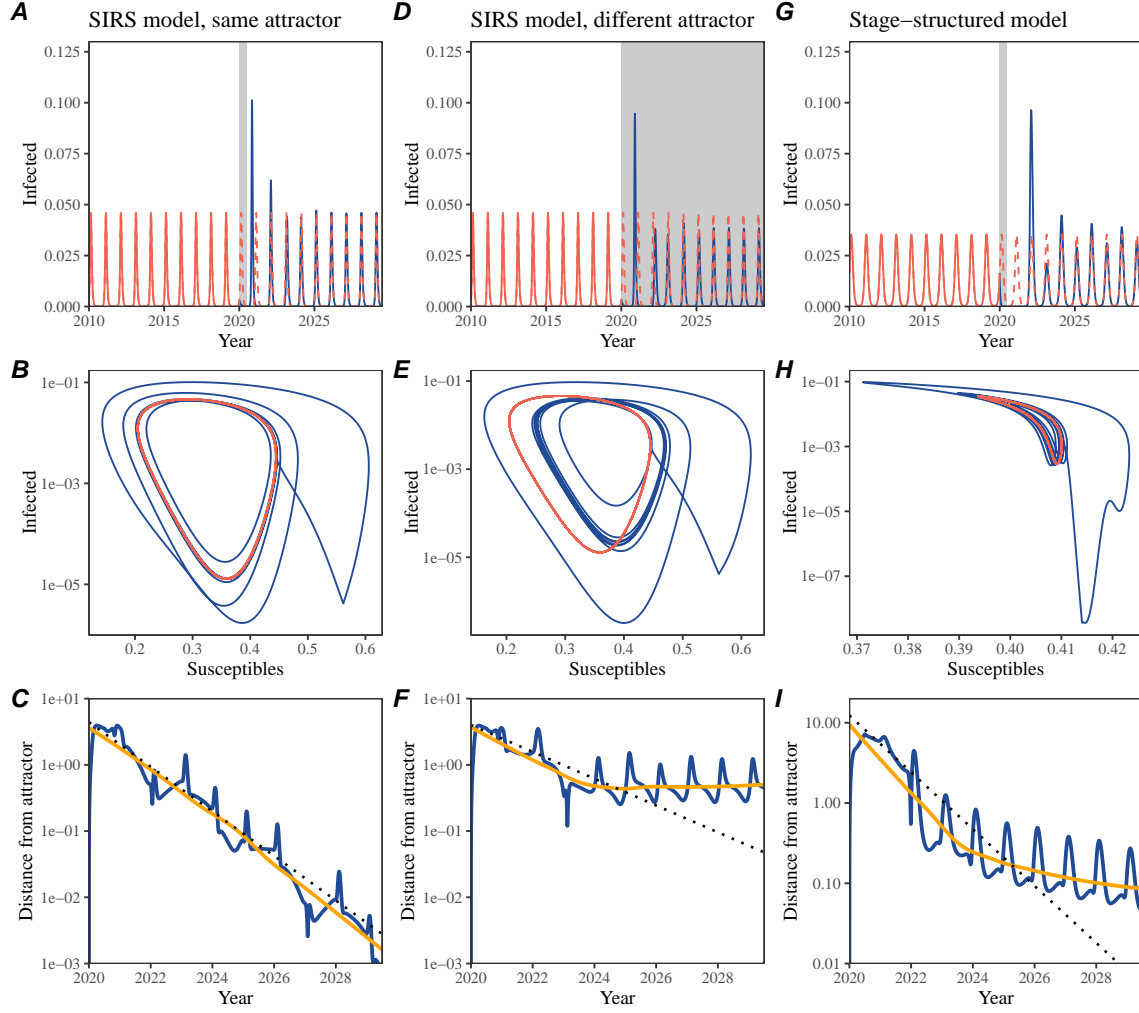


Figure 2: A simple method to measure pathogen resilience following NPIs across different scenarios. (A, D, G) Simulated epidemic trajectories across various models. Red and blue solid lines represent epidemic dynamics before and after interventions are introduced, respectively. Red dashed lines represent counterfactual epidemic dynamics in the absence of interventions. Gray regions indicate the duration of interventions. (B, E, H) Phase plane representation of the time series in panels A, D, and G alongside the corresponding susceptible host dynamics. Red and blue solid lines represent epidemic trajectories on an SI phase plane before and after interventions are introduced, respectively. (C, F, I) Changes in logged distance from the attractor over time. Blue lines represent the logged distance from the attractor. Orange lines represent the locally estimated scatterplot smoothing (LOESS) fits to the logged distance from attractor. Dotted lines show the intrinsic resilience of the seasonally unforced system.

116 decreases exponentially at a rate that is consistent with the intrinsic resilience of

117 the seasonally unforced stage-structured system, but the rate of decrease decelerates
118 with the damped oscillations (Figure 2I). This behavior is also referred to as a ghost
119 attractor, which causes long transient dynamics and slow transitions [16]. Strong
120 seasonal forcing in transmission can also lead to transient phenomena for a simple
121 SIRS model, causing a slow return to pre-perturbation dynamics (Supplementary
122 Figure S1).

123 This empirical approach allows us to measure the resilience of a two-strain host-
124 pathogen system even when we have incomplete observation of the infection dynam-
125 ics. Simulations from a simple two-strain system illustrate that separate analyses of
126 individual strain dynamics (e.g., RSV A vs B) and a joint analysis of total infections
127 (e.g., total RSV infections) yield identical resilience estimates (Supplementary Fig-
128 ure S2, 3). This is expected because the dynamics of two strains (or two pathogens)
129 around the attractor in a coupled system are described by the same set of eigen-
130 values and eigenvectors, meaning that both strains should exhibit identical rates of
131 returns following a perturbation. Analogous to a single system, strong seasonal forc-
132 ing in transmission can cause the system to slow down through transient phenomena
133 (Supplementary Figure S4).

134 These observations indicate three possibilities. First, we can directly estimate the
135 empirical resilience of a host-pathogen system by measuring the rate at which the
136 system approaches an attractor, provided that we have a way to quantify the distance
137 from the attractor. The empirical approach to estimating pathogen resilience is
138 particularly convenient because it does not require us to know the true underlying
139 model; estimating the intrinsic resilience from fitting misspecified models can lead
140 to biased estimates (Supplementary Figure S5). Second, resilience estimates allow
141 us to make phenomenological predictions about the dynamics of a host-pathogen
142 system following a perturbation. Assuming that the distance from the attractor
143 will decrease exponentially over time, we can obtain a ballpark estimate for when
144 the system will reach an attractor. Finally, a change in the rate of an exponential
145 decrease in the distance from attractor can provide information about whether the
146 system has reached an alternative attractor, or a ghost attractor, that is different
147 from the original, pre-pandemic attractor. These alternative attractors may reflect
148 continued perturbations from permanent changes in transmission patterns as well as
149 changes in immune landscapes.

150 **Inferring pathogen resilience from real data**

151 Based on these observations, we now lay out our approach to estimating pathogen
152 resilience from real data (Figure 3). We then test this approach against simulations
153 and apply it to real data.

154 So far, we focused on simple examples that assume a constant transmission re-
155 duction. However, in practice, the impact of NPIs on pathogen transmission is likely
156 more complex (Figure 3A), reflecting introduction and relaxation of various inter-

vention strategies. In some cases, strong NPIs can even lead to a local fadeout, requiring immigration from another location for epidemic re-emergence. These complexities can lead to longer delays between the introduction of NPIs and pathogen re-emergence as well as temporal variation in outbreak sizes (Figure 3B): in this example, continued transmission reduction from NPIs limits the size of the first outbreak in 2021 following the emergence, allowing for a larger outbreak in 2022 when NPIs are further relaxed.

Previously, we relied on the dynamics of susceptible and infected hosts to compute the distance from attractor (Figure 2), but information on susceptible hosts is rarely available in practice. In addition, uncertainties in case counts due to observation error as well as the possibility of complex, multiannual attractor add challenges to measuring the distance from attractor. To address these challenges, we first reconstruct an empirical attractor by utilizing Takens' theorem, which states that an attractor of a nonlinear multidimensional system can be mapped onto a delayed embedding [14]. Here, we use delayed logged values of pre-pandemic cases $C(t)$ (Figure 3C) to reconstruct the attractor:

$$\langle \log(C(t) + 1), \log(C(t - \tau) + 1), \dots, \log(C(t - (M - 1)\tau) + 1) \rangle, \quad (1)$$

where the delay τ and embedding dimension M are determined based on autocorrelations and false nearest neighbors, respectively [17, 18]. We then apply the same delay and embedding dimensions to the entire time series to determine the position on a multi-dimensional state space (Figure 3D), which allows us to measure the nearest neighbor distance between the current state of the system and the empirical pre-pandemic attractor (Figure 3E). In principle, we can quantify how fast this distance decreases by fitting a linear regression on a log scale, where the slope of the linear regression corresponds to pathogen resilience. Overall temporal variations in the distance from attractor, especially the observed rate of decrease, appear robust to choices about embedding delays and dimensions; using longer delays and higher dimensions tends to smooth out temporal variations in the distance from the attractor (Supplementary Figure S6).

Complex changes in the distance from attractor suggest that estimating pathogen resilience from linear regression will likely be sensitive to our choice of fitting windows for the regression (Figure 3E). In Supplementary Materials, we explore an automated window selection criterion for linear regression and test it against randomized, stochastic simulations across a wide range of realistic NPI shapes. We find that resilience estimates based on the automated window selection criterion are moderately correlated ($\rho = 0.48$) with the intrinsic resilience of the post-NPI attractor (Supplementary Figure S7). In contrast, a naive approach that uses the entire time series, starting from the peak distance, only gives a correlation coefficient of $\rho = 0.09$ and consistently underestimates the intrinsic resilience (Supplementary Figure S7).

Now, we apply this approach to pathogen surveillance data presented in Figure 1. For each time series, we apply Takens' theorem independently to reconstruct the empirical attractor and obtain the corresponding time series of distances from

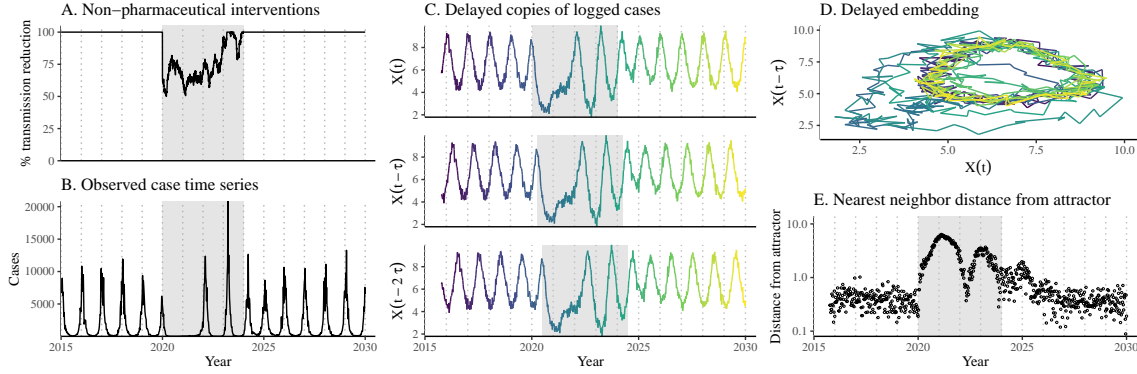


Figure 3: **A schematic diagram explaining the inference of pathogen resilience from synthetic data.** (A) A realistic example of simulated NPIs, represented by a relative reduction in transmission. (B) The impact of the synthetic NPI on epidemic dynamics simulated using a SIRS model with demographic stochasticity. (C) Generating delayed copies of the logged time series allows us to obtain an embedding. (D) Two dimensional representation of an embedding. (E) Delayed embedding allows us to calculate the nearest neighbor distance from the empirical attractor, which is determined based on the pre-pandemic time series. This distance time series can be used to infer pathogen resilience after choosing an appropriate window for linear regression.

198 attractors (Supplementary Figure S8 for the distance time series and linear regression
 199 fits). Then, we use the automated window selection criterion to fit a linear regression
 200 and estimate the empirical resilience for each pathogen in each country. For most
 201 respiratory pathogens, resilience estimates fall between 0.4/year and 1.8/year (Figure
 202 4A), with the exception of rhinovirus in the US (0.066/year; 95% CI: 0.018/year–
 203 0.113/year) and bocavirus in Korea (0.087/year; 95% CI: 0.023/year–0.151/year).
 204 Excluding these exceptions, the mean resilience of common respiratory pathogens
 205 is 0.974/year (95% CI: 0.784/year–1.16/year). As a reference, this is ≈ 7 times
 206 higher than the intrinsic resilience of pre-vaccination measles in England and Wales
 207 (≈ 0.13 /year). Finally, resilience estimates for norovirus appears to be comparable
 208 to the intrinsic resilience of measles: 0.119/year (95%CI: 0.004/year–0.233/year) for
 209 Korea and 0.385/year (95% CI: 0.167/year–0.603/year). A simple ANOVA shows
 210 that there are significant differences in resilience estimates across countries ($p <$
 211 0.036) and pathogens ($p < 0.030$).

212 Using resilience estimates, we now predict when each pathogen would hypothet-
 213 ically return to their pre-pandemic dynamics, assuming no long-term change in the
 214 attractor. Specifically, we extend our linear regression fits to distance-from-attractor
 215 time series and ask when the predicted regression line will cross a threshold value,
 216 which we set equal to the mean of pre-pandemic distances. We predict that a re-
 217 turn to pre-pandemic cycles would be imminent for most pathogens (Figure 4B; see
 218 Supplementary Figure S9 for a zoomed out version). We also predict that many

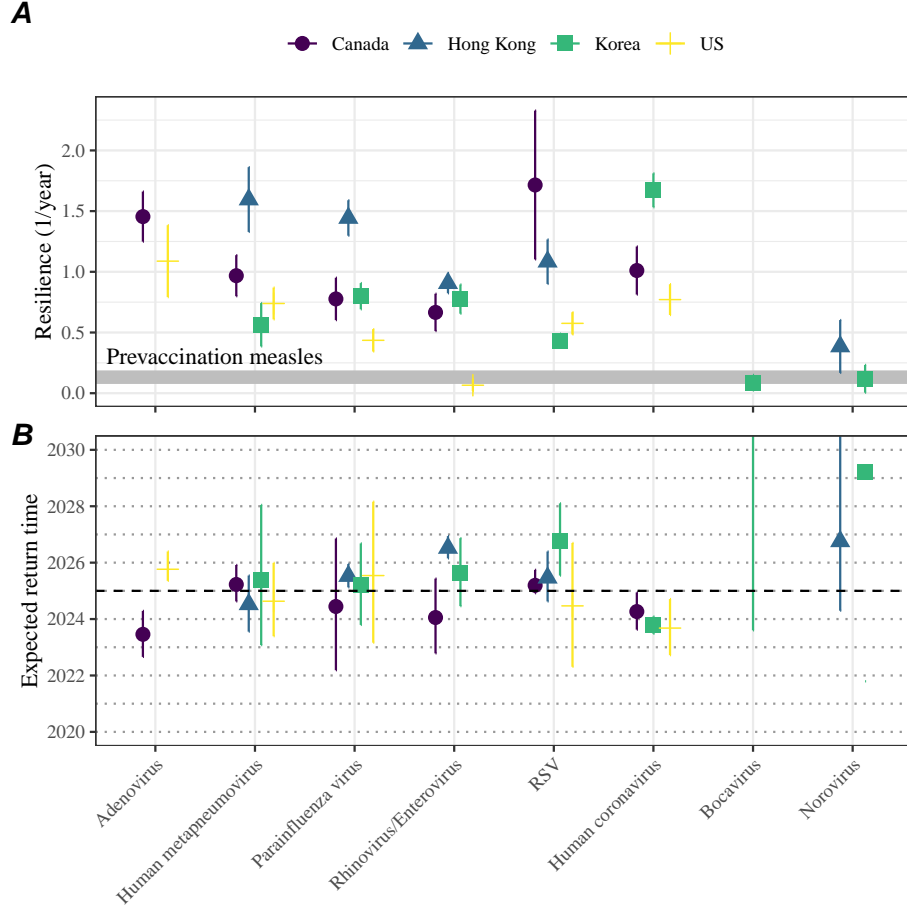


Figure 4: **Summary of resilience estimates.** (A) Estimated pathogen resilience. The gray horizontal line represents the intrinsic resilience of pre-vaccination measles dynamics. (B) Predicted timing of when each pathogen will return to their pre-pandemic cycles. The dashed line in panel B indicates the end of 2024 (current observation time). Error bars represent 95% confidence intervals.

pathogens should have already returned to their pre-pandemic dynamics by the end of 2024, but these predictions contradict some of the observed pathogen dynamics. For example, we predict that both human metapneumovirus and RSV in Korea should have returned to their attractors by now, but the magnitude and timing of recent epidemics are different from pre-pandemic patterns (Figure 1). These observations suggest the possibility that some common respiratory pathogens may have converged to different attractors.

In Supplementary Materials, we also consider using a lower threshold for the false nearest neighbor approach when determining the embedding dimension; this gives a higher embedding dimension. As explained earlier (Supplementary Figure S6), this gives a smoother distance-from-attractor time series (compare Supplementary Figure

230 S10 with S8); this also requires us to use longer time series, which prevents us from
 231 estimating resilience for some pathogens. Overall, resulting estimates of pathogen
 232 resilience with higher embedding dimensions still mostly fall between 0.3/year and
 233 2.1/year (Supplementary Figure S11). A direct comparison between two approaches
 234 (i.e., original estimate vs using higher dimensions) shows a strong consistency in
 235 resilience estimates (Supplementary Figure S12).

236 **Susceptible host dynamics explain variation in pathogen 237 resilience**

238 So far, we focused on quantifying pathogen resilience from the observed patterns of
 239 pathogen re-emergence following NPIs. But what factors determine how resilient a
 240 host-pathogen system is? Here, we use the SIRS model to show that susceptible host
 241 dynamics are the key determinants of pathogen resilience. To do so, we vary the
 242 basic reproduction number \mathcal{R}_0 , which represents the average number of secondary
 243 infections caused by a newly infected individual in a fully susceptible population,
 244 and the duration of immunity and compute intrinsic resilience for each parameter.

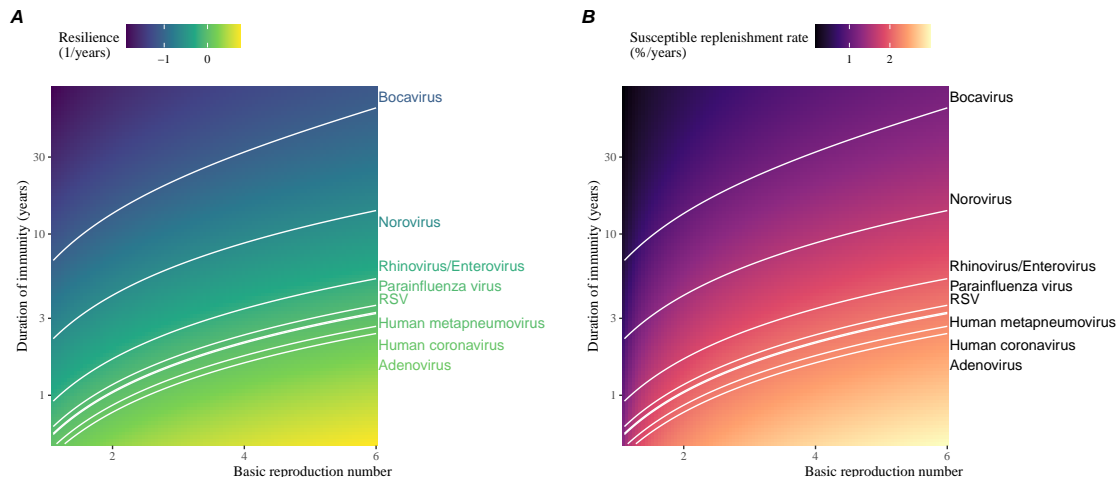


Figure 5: Linking pathogen resilience to epidemiological parameters and susceptible host dynamics. (A) The heat map represents intrinsic resilience as a function of the basic reproduction number \mathcal{R}_0 and the duration of immunity. (B) The heat map represents per-capita susceptible replenishment rate as a function of the basic reproduction number \mathcal{R}_0 and the duration of immunity. The standard SIRS model is used to compute intrinsic resilience and per-capita susceptible replenishment rate. Lines correspond to a set of parameters that are consistent with mean resilience estimates for each pathogen. Pathogens are ranked based on their mean resilience estimates, averaged across different countries.

245 We find an increase in \mathcal{R}_0 and a decrease in duration of immunity correspond
246 to an increase in pathogen resilience (Figure 5A). These variations can be under-
247 stood in terms of the susceptible host dynamics, where faster per-capita susceptible
248 replenishment rate causes the system to be more resilient (Figure 5B). This rate can
249 be expressed as a ratio between absolute rate at which new susceptibles enter the
250 population and the equilibrium number of susceptible individuals in the population,
251 \bar{S} . Therefore, both higher \mathcal{R}_0 and shorter duration of immunity can drive faster
252 per-capita susceptible replenishment rate (Figure 5B), especially because higher \mathcal{R}_0
253 leads to lower \bar{S} .

254 Finally, we can rank different pathogens based on the average values of empirical
255 resilience computed previously, which allows us to determine a set of parameters that
256 are consistent with the estimated resilience (Figure 5A). Across all pathogens we
257 consider, except for bocavirus and norovirus, we estimate that the average duration
258 of immunity is likely to be short (< 6 years) across a plausible range of \mathcal{R}_0 . These
259 rankings further allow us to map each pathogen onto a set of SIRS parameters that
260 are consistent with its empirical resilience (Figure 5A) and obtain a plausible range
261 of susceptible replenishment rates for each pathogen (Figure 5B). However, we note
262 that there is no one-to-one correspondence between susceptible replenishment rates
263 and pathogen resilience, leading to a wide uncertainty in the estimates for susceptible
264 replenishment rates (Figure 5B).

265 Discussion

266 The pandemic NPIs have caused major disruptions to circulation patterns of both
267 respiratory and non-respiratory pathogens, adding challenges to predicting their fu-
268 ture dynamics [1, 2, 3, 4]. However, these NPIs offer large-scale natural experiments
269 for understanding how different pathogens respond to perturbations. In this study,
270 we show that pathogen re-emergence patterns following NPIs can be characterized
271 through the lens of ecological resilience. Traditionally, ecological resilience measures
272 how fast a system returns to a reference state following a perturbation. In the con-
273 text of respiratory pathogens, resilience measures how fast epidemics return to their
274 endemic cycles after NPIs are lifted.

275 We use an attractor reconstruction approach to quantify how distance from at-
276 tractor changes over time for each pathogen [14]. We show that the resilience of
277 a host-pathogen system can be estimated by fitting a linear regression to a logged
278 distance-from-attractor time series. Overall, we estimate that the resilience for most
279 common respiratory pathogens ranges between 0.4/year and 1.8/year, which is 3–14
280 times more resilient than prevaccination measles, indicating potential challenges in
281 controlling common respiratory pathogens.

282 Our framework allows us to make phenomenological predictions about when each
283 pathogen will return to their endemic cycles. The ability to predict future epidemic
284 patterns from resilience estimates offers a new paradigm for epidemic forecasting.

285 While this approach cannot predict the exact timing of outbreaks or epidemic pat-
286 terns, it is nonetheless useful for predicting when epidemics will settle down to regular
287 cycles after a large perturbation, such as pandemic NPIs.

288 Our analyses suggest a possibility that several pathogens may have converged
289 to different endemic cycles compared to their pre-pandemic epidemic patterns. Key
290 examples include human metapnuemovirus, RSV, and bocavirus in Korea as well as
291 RSV in Hong Kong. These changes may reflect changes in surveillance or actual shift
292 in the dynamics, caused by permanent changes in behavior or population-level immu-
293 nity. While it seems unlikely that permanent changes in behavior would only affect a
294 few pathogens and not others, we cannot rule out this possibility given heterogeneity
295 in the age of infection across different respiratory pathogens [SWP: CITE]. A shift
296 in population-level immunity is plausible, as the emergence of SARS-CoV-2 and ex-
297 tinction of influenza B/Yamagata likely caused major changes in immune landscapes;
298 interactions among co-circulating pathogens, such as cross immunity between RSV
299 and HMPV [19], may have also contributed to changes in population-level immu-
300 nity. However, we currently do not know how immunity, or lack thereof, from these
301 pathogens would affect infection from other pathogens. Future studies should use
302 detailed mechanistic models, coupled with behavioral and immunological data, to
303 test these hypotheses and better understand post-pandemic dynamics of endemic
304 pathogens.

305 We show that susceptible host dynamics shape pathogen resilience, where faster
306 replenishment of the susceptible population causes the pathogen to be more resilient.
307 For simplicity, we focus on waning immunity and birth as the main drivers of the
308 susceptible host dynamics but other mechanisms can also contribute to the replen-
309 ishment of the susceptible population. In particular, pathogen evolution, especially
310 the emergence of antigenically novel strains, can cause effective waning of immunity
311 in the population; therefore, we hypothesize that faster rates of antigenic evolution
312 can also cause a pathogen to be more resilient. Future studies should explore the
313 relationship between the rate of evolution and resilience for antigenically evolving
314 pathogens.

315 Quantifying pathogen resilience also offers novel approaches to validating population-
316 level epidemiological models. So far, most of model validation in infectious disease
317 ecology is based on the ability of a model to reproduce the observed epidemic dy-
318 namics and to predict future dynamics [20, 19, 21, 22, 23]. However, many models
319 can perform similarly under these criteria. For example, two major RSV models have
320 been proposed to explain biennial epidemic patterns: (1) a stage- and age-structured
321 model that allows disease severity to vary with number of past infections and age of
322 infection [21] and (2) a pathogen-interaction model that accounts for cross immunity
323 between RSV and human metapnuemovirus [19]. Since both models can accurately
324 reproduce the observed epidemic patterns, standard criteria for model validation do
325 not allow us to distinguish between these two models from population-level data
326 alone. Instead, we can measure the empirical resilience of each model by simulating
327 various perturbations and compare them to estimates of empirical resilience from

328 data, using pandemic NPIs as an opportunity.

329 There are several limitations to our work. First, we did not extensively explore
330 other approaches to reconstructing the attractor. Recent studies showed that more
331 sophisticated approaches, such as using non-uniform embedding, can provide more
332 robust reconstruction for noisy data [18]. In the context of causal inference, choices
333 about embedding can have major impact on the resulting inference [24]. Our re-
334 silience estimates are likely overly confident given a lack of uncertainties in attractor
335 reconstruction as well as the simplicity of our statistical framework. Short pre-
336 pandemic time series also contribute to the crudeness of our estimates. Nonetheless,
337 as illustrated in our sensitivity analyses (Supplementary Figure S6, S10–S12), infer-
338 ences about pathogen resilience in our SIRS model appear to be robust to decisions
339 about embedding lags and dimensions—this is because tracking the rate at which
340 the system approaches the attractor is likely a much simpler problem than making
341 inferences about causal directionality. Our qualitative prediction that common res-
342 piratory pathogens are more resilient than prevaccination measles is also likely to be
343 robust to these predictions, given how rapid many respiratory pathogens returned to
344 their original cycles following pandemic NPIs.

345 Predicting the impact of anthropogenic changes on infectious disease dynamics
346 is a fundamental aim of infectious disease research in a rapidly changing world. Our
347 study illustrates that quantifying pathogen resilience can help us understand how
348 infectious disease pathogens respond to major perturbations caused by NPIs. More
349 broadly, a detailed understanding of the determinants of pathogen resilience may
350 offer unique insights into pathogen persistence and controllability.

351 Materials and Methods

352 Data

353 We gathered time series on respiratory infections from Canada, Hong Kong, Korea,
354 and United States (US). As a reference, we also included time series data on norovirus
355 infections for available countries—in contrast to respiratory pathogens, we expect
356 gastrointestinal viruses, such as norovirus, to be differently affected by pandemic
357 NPIs. For all time series, we rounded every year to 52 weeks by taking the average
358 number of cases and tests between the 52nd and 53rd week. We also rescale all time
359 series to account for changes in testing patterns, which are then used for the actual
360 analysis.

361 Weekly time series of respiratory infection cases in Canada comes from the Res-
362piratory Virus Detection Surveillance System, which collect data from select labo-
363ratories across Canada. We extracted the data from <https://www.canada.ca/en/public-health/services/surveillance/respiratory-virus-detections-canada.html>.
364 To account for an increase in testing from 2013 to 2024, we calculate a 2 year
365 moving average for the number of tests for each pathogen, which we use as a proxy
366 for testing effort. Then, we divide the smoothed testing patterns by the smoothed
367

368 value at the final week such that the testing effort has a maximum of 1. We then
369 divide weekly cases by the testing effort to obtain a scaled case time series. A similar
370 approach was used earlier for the analysis of RSV time series in the US [21].

371 Weekly time series of respiratory infection cases in Hong Kong comes from the
372 Centre for Health Protection, Department of Health. We extract the data from
373 <https://www.chp.gov.hk/en/statistics/data/10/641/642/2274.html>. We also
374 apply the same scaling procedure to the time series as we did for Canada. For Hong
375 Kong, we only adjust for testing efforts up to the end of 2019 because there was a
376 major reduction in testing for common respiratory pathogens since 2020.

377 Weekly time series of acute respiratory infection cases in Korea comes from Ko-
378 rea Disease Control and Prevention Agency. We extract the data from <https://dportal.kdca.go.kr/pot/is/st/ari.do>. While we do not have information on
379 testing, the reported number of respiratory infections consistently increased from
380 2013 to the end of 2019, which we interpreted as changes in testing patterns. Since
381 we do not have testing numbers, we used the weekly sum of all acute respiratory vi-
382 ral infection cases as a proxy for testing, which were further smoothed with moving
383 averaged and scaled to have a maximum of 1. For Korea, we also only adjust for
384 testing efforts up to the end of 2019.

385 Finally, weekly time series of respiratory infection cases in the US comes from
386 the National Respiratory and Enteric Virus Surveillance System. In the US, there
387 has been a large increase in testing against some respiratory pathogens, especially
388 RSV, which could not be corrected for through simple scaling. Instead, we derive an
389 incidence proxy by multiplying the test positivity with influenza-like illness positivity,
390 which is taken from <https://gis.cdc.gov/grasp/fluview/fluportaldashboard.html>. This method of estimating an incidence proxy has been recently applied in
391 the analysis of seasonal coronaviruses [7] and *Mycoplasma pneumoniae* infections [4].
392 Detailed assumptions and justifications are provided in [25].

395 Estimating pathogen resilience

396 In order to measure pathogen resilience from surveillance data, we first reconstruct
397 the empirical pre-pandemic attractor of the system using Takens' embedding theorem
398 [14]. Specifically, for a given pathogen, we take the pre-pandemic (before 2020)
399 case time series $C(t)$ and reconstruct the attractor using delayed embedding with a
400 uniform delay of τ and dimension M :

$$X_{\tau,m}(t) = \langle \log(C(t) + 1), \log(C(t - \tau) + 1), \dots, \log(C(t - (M - 1)\tau) + 1) \rangle. \quad (2)$$

401 Here, the delay τ is determined by calculating the autocorrelation of the logged pre-
402 pandemic time series and asking when the autocorrelation crosses 0 for the first time
403 [18]; a typical delay for an annual outbreak is around 13 weeks.

404 Then, for a given delay τ , we determine the embedding dimension M using the
405 false nearest neighbors approach [17, 18]. To do so, we start with an embedding
406 dimension e and construct a set of points $A_{\tau,e} = \{X_{\tau,e}(t) | t < 2020\}$. Then, for

407 each point $X_{\tau,e}(t)$, we determine the nearest neighbor from the set $A_{\tau,e}$, which we
 408 denote $X_{\tau,e}(t_{nn})$ for $t \neq t_{nn}$. Then, if the distance between these two points on $e+1$
 409 dimension, $D_{\tau,e+1}(t) = \|X_{\tau,e+1}(t_{nn}) - X_{\tau,e+1}(t)\|_2$, is larger than their distance on
 410 e dimension, $D_{\tau,e}(t) = \|X_{\tau,e}(t_{nn}) - X_{\tau,e}(t)\|_2$, these two points are deemed to be
 411 false nearest neighbors; specifically, we use a threshold R for the ratio between two
 412 distances $D_{\tau,e+1}(t)/D_{\tau,e}(t)$ to determine false nearest neighbors. In the main text, we
 413 determine the embedding dimension based on the first dimension without any false
 414 nearest neighbors for $R = 10$. In Supplementary Materials, we impose $R = 5$ to select
 415 for higher dimensions. Once we determine the embedding lag τ and dimension M ,
 416 we apply the embedding to the entire time series and calculate the nearest neighbor
 417 distance against the attractor $A_{\tau,M}$ to obtain a time series of distance from attractor
 418 $D_{\tau,M}(t)$.

419 From a time series of distances from the attractor, we estimate pathogen resilience
 420 by fitting a linear regression to an appropriate window. To automatically select
 421 the fitting window, we begin by smoothing the distance time series using locally
 422 estimated scatterplot smoothing (LOESS) to obtain $\hat{D}_{\tau,M}(t)$, where the smoothing
 423 is performed on a log scale and exponentiated afterwards. Then, we determine
 424 threshold values (T_{start} and T_{end}) for the smoothed distances and choose the fitting
 425 window based on when $\hat{D}_{\tau,M}(t)$ crosses these threshold values for the first time.
 426 These thresholds are determined by first calculating maximum distance,

$$\max \hat{D} = \max \hat{D}_{\tau,M}(t), \quad (3)$$

427 and mean pre-pandemic distance,

$$\hat{D}_{\text{mean}} = \frac{1}{N_{t < 2020}} \sum_{t < 2020} \hat{D}_{\tau,M}(t), \quad (4)$$

428 as a reference, and then dividing their ratios into 10 equal bins:

$$T_{\text{start}} = \hat{D}_{\text{mean}} \times \left(\frac{\max \hat{D}}{\hat{D}_{\text{mean}}} \right)^{9/10} \quad (5)$$

$$T_{\text{end}} = \hat{D}_{\text{mean}} \times \left(\frac{\max \hat{D}}{\hat{D}_{\text{mean}}} \right)^{1/10} \quad (6)$$

429 This allows us to discard the initial period during which the distance increases (from
 430 the introduction of intervention measures) and the final period during which the
 431 distance plateaus (as the system reaches an attractor). The fitting window is deter-
 432 mined based on when the smoothed distance $\hat{D}_{\tau,M}(t)$ crosses these threshold values
 433 for the first time; then, we fit a linear regression to logged (unsmoothed) distances
 434 $\log D_{\tau,M}(t)$ using that window.

435 **Mathematical modeling**

436 Throughout the paper, we use a series of mathematical models to illustrate the con-
 437 cept of pathogen resilience and to understand the determinants of pathogen resilience.
 438 In general, the intrinsic resilience for a given system is given by the largest real part
 439 of the eigenvalues of the linearized system at endemic equilibrium. Here, we focus on
 440 the SIRS model with demography and present the details of other models in Supple-
 441 mentary Materials. The SIRS (Susceptible-Infected-Recovered-Susceptible) model is
 442 the simplest model that allows for waning of immunity, where recovered (immune)
 443 individuals are assumed to become fully susceptible after an average of $1/\delta$ time pe-
 444 riod. The dynamics of the SIRS model is described by the following set of differential
 445 equations:

$$\frac{dS}{dt} = \mu - \beta(t)SI - \mu S + \delta R \quad (7)$$

$$\frac{dI}{dt} = \beta(t)SI - (\gamma + \mu)I \quad (8)$$

$$\frac{dR}{dt} = \gamma I - (\delta + \mu)R \quad (9)$$

$$(10)$$

446 where μ represents the birth/death rate, $\beta(t)$ represents the time-varying trans-
 447 mission rate, and γ represents the recovery rate. The basic reproduction number
 448 $\mathcal{R}_0(t) = \beta(t)/(\gamma + \mu)$ is defined as the average number of secondary infections that
 449 a single infected individual would cause in a fully susceptible population at time t
 450 and measures the intrinsic transmissibility of a pathogen.

451 When we first introduce the idea of pathogen resilience (Figure 2), we impose
 452 sinusoidal changes to the transmission rate to account for seasonal transmission:

$$\beta(t) = b_1(1 + \theta \cos(2\pi(t - \phi)))\alpha(t), \quad (11)$$

453 where b_1 represents the baseline transmission rate, θ represents the seasonal am-
 454 plitude, and ϕ represents the seasonal offset term. Here, we also introduce an ex-
 455 tra multiplicative term $\alpha(t)$ to account for the impact of pandemic NPIs, where
 456 $\alpha(t) < 1$ indicates transmission reduction. Figure 2A and 2B are generated assum-
 457 ing $b_1 = 3 \times (365/7 + 1/50)/\text{years}$, $\theta = 0.2$, $\phi = 0$, $\mu = 1/50/\text{years}$, $\gamma = 365/7/\text{years}$,
 458 and $\delta = 1/2/\text{years}$. In Figure 2A, we impose a 50% transmission reduction for 6
 459 months from 2020:

$$\alpha(t) = \begin{cases} 0.5 & 2020 \leq t < 2020.5 \\ 1 & \text{otherwise} \end{cases} \quad (12)$$

460 In Figure 2B, we impose a 50% transmission reduction for 6 months from 2020 and
 461 a permanent 10% reduction onward:

$$\alpha(t) = \begin{cases} 1 & t < 2020 \\ 0.5 & 2020 \leq t < 2020.5 \\ 0.9 & 2020.5 \leq t \end{cases} \quad (13)$$

462 In both scenarios, we simulate the SIRS model from the following initial conditions
463 ($S(0) = 1/\mathcal{R}_0$, $I(0) = 1 \times 10^{-6}$, and $R(0) = 1 - S(0) - I(0)$) from 1900 until 2030.

464 To measure the empirical resilience of the SIR model (Figure 2C and 2F), we
465 compute the normalized distance between post-intervention susceptible and logged
466 infected proportions and their corresponding pre-intervention values at the same time
467 of year:

$$\sqrt{\left(\frac{S(t) - S_{\text{pre}}(t)}{\sigma_S}\right)^2 + \left(\frac{\log I(t) - \log I_{\text{pre}}(t)}{\sigma_{\log I}}\right)^2}, \quad (14)$$

468 where σ_S and $\sigma_{\log I}$ represent the standard deviation in the pre-intervention suscep-
469 tible and logged infected proportions. We normalize the differences in susceptible
470 and logged infected proportions to allow both quantities to equally contribute to the
471 changes in distance from attractor. We used logged prevalence, instead of absolute
472 prevalence, in order to capture epidemic dynamics in deep troughs during the in-
473 tervention period. In Supplementary Materials, we also compare how the degree of
474 seasonal transmission affects empirical resilience by varying θ from 0 to 0.4; when
475 we assume no seasonality ($\theta = 0$), we do not normalize the distance because the
476 standard deviation of pre-intervention dynamics are zero.

477 Finally, we use the SIRS model to understand how underlying epidemiological
478 parameters affect pathogen resilience and link this relationship to underlying sus-
479 ceptible host dynamics. For the simple SIRS model without seasonal transmission
480 ($\theta = 0$), the intrinsic resilience corresponds to

$$-\frac{\text{Re}(\lambda)}{2} = \frac{\delta + \beta I^* + \mu}{2}. \quad (15)$$

481 Here, I^* represents the prevalence at endemic equilibrium:

$$I^* = \frac{(\delta + \mu)(\beta - (\gamma + \mu))}{\beta(\delta + \gamma + \mu)}. \quad (16)$$

482 The susceptible replenishment rate is given by

$$S_{\text{replenish}} = \frac{\mu + \delta R}{S^*}, \quad (17)$$

483 where $S^* = 1/\mathcal{R}_0$ represents the equilibrium proportion of susceptible individuals.
484 We vary the basic reproduction number \mathcal{R}_0 between 1.1 to 6 and the average duration
485 of immunity $1/\delta$ between 2 to 80 years, and compute these two quantities. In doing
486 so, we fix all other parameters: $\mu = 1/80/\text{years}$ and $\gamma = 365/7/\text{years}$.

487 Data availability

488 Funding

489 **Supplementary Text**

490 **Resilience of a stage-structured system.**

491 In Figure 2G–I, we use a more realistic, stage-structured model to illustrate how
 492 transient phenomena can cause the system to slow down. Specifically, we use the
 493 stage-structured RSV model proposed by [21], which assumes that subsequent rein-
 494 fections cause an individual to become less susceptible and transmissible than previ-
 495 ous infections. The model dynamics can be described as follows:

$$\frac{dM}{dt} = \mu - (\omega + \mu)M \quad (S1)$$

$$\frac{dS_0}{dt} = \omega M - (\lambda(t) + \mu)S_0 \quad (S2)$$

$$\frac{dI_1}{dt} = \lambda(t)S_0 - (\gamma_1 + \mu)I_1 \quad (S3)$$

$$\frac{dS_1}{dt} = \gamma_1 I_1 - (\sigma_1 \lambda(t) + \mu)S_1 \quad (S4)$$

$$\frac{dI_2}{dt} = \sigma_1 \lambda(t)S_1 - (\gamma_2 + \mu)I_2 \quad (S5)$$

$$\frac{dS_2}{dt} = \gamma_2 I_2 - (\sigma_2 \lambda(t) + \mu)S_2 \quad (S6)$$

$$\frac{dI_3}{dt} = \sigma_2 \lambda(t)S_2 - (\gamma_3 + \mu)I_3 \quad (S7)$$

$$\frac{dS_3}{dt} = \gamma_3 I_3 - (\sigma_3 \lambda(t) + \mu)S_3 + \gamma_4 I_4 \quad (S8)$$

$$\frac{dI_4}{dt} = \sigma_3 \lambda(t)S_3 - (\gamma_4 + \mu)I_4 \quad (S9)$$

$$(S10)$$

496 where M represents the proportion of individuals who are maternally immune; S_i
 497 represents the proportion of individuals who are susceptible after i prior infections; I_i
 498 represents the proportion of individuals who are currently (re)-infected with their i -th
 499 infection; μ represents the birth and death rates; $1/\omega$ represents the mean duration
 500 of maternal immunity; $1/\gamma_i$ represents the mean duration of infection; $\lambda(t)$ represents
 501 the force of infection; and σ_i represents the reduction in susceptibility for the i -th
 502 reinfection. The force of infection is modeled using a sinusoidal function:

$$\beta(t) = b_1(1 + \theta \cos(2\pi(t - \phi)))\alpha(t) \quad (S11)$$

$$\lambda(t) = \beta(I_1 + \rho_1 I_2 + \rho_2(I_3 + I_4)), \quad (S12)$$

503 where b_1 represents the baseline transmission rate; θ represents the seasonal ampli-
 504 tude; ϕ represents the seasonal offset term; $\alpha(t)$ represents the intervention effect;
 505 and ρ_i represents the impact of immunity on transmission reduction. We use the

506 following parameters to simulate the impact of interventions on epidemic dynam-
 507 ics [21]: $b_1 = 9 \times (365/10 + 1/80)/\text{years}$, $\theta = 0.2$, $\phi = -0.1$, $\omega = 365/112/\text{years}$,
 508 $\gamma_1 = 365/10/\text{years}$, $\gamma_2 = 365/7/\text{years}$, $\gamma_3 = 365/5/\text{years}$, $\sigma_1 = 0.76$, $\sigma_2 = 0.6$,
 509 $\sigma_3 = 0.4$, $\rho_1 = 0.75$, $\rho_2 = 0.51$, and $\mu = 1/80/\text{years}$. We assume a 50% transmission
 510 reduction for 6 months from 2020:

$$\alpha(t) = \begin{cases} 0.5 & 2020 \leq t < 2020.5 \\ 1 & \text{otherwise} \end{cases} \quad (\text{S13})$$

511 The model is simulated from 1900 to 2030 using the following initial conditions:
 512 $M = 0$, $S_0 = 1/\mathcal{R}_0 - I_1$, $I_1 = 1 \times 10^{-6}$, $S_1 = 1 - 1/\mathcal{R}_0$, $I_2 = 0$, $S_2 = 0$, $I_3 = 0$,
 513 $S_3 = 0$, and $I_4 = 0$. For the phase plane analysis (Figure 2H) and distance analysis
 514 (Figure 2I), we rely on the average susceptibility,

$$\bar{S} = S_0 + \sigma_1 S_1 + \sigma_2 S_2 + \sigma_3 S_3, \quad (\text{S14})$$

515 and total prevalence,

$$I_{\text{total}} = I_1 + I_2 + I_3 + I_4. \quad (\text{S15})$$

516 These quantities are used to compute the normalized distance from the attractor, as
 517 described in the main text.

518 Resilience of a multistain system.

519 We use a simple two-strain model to show that a multistain host-pathogen system
 520 that is coupled through cross immunity can be described by a single resilience value.
 521 The model dynamics can be described as follows [19]:

$$\frac{dS}{dt} = \mu - \mu S - (\lambda_1 + \lambda_2)S + \rho_1 R_1 + \rho_2 R_2 \quad (\text{S16})$$

$$\frac{dI_1}{dt} = \lambda_1 S - (\gamma_1 + \mu)I_1 \quad (\text{S17})$$

$$\frac{dI_2}{dt} = \lambda_2 S - (\gamma_2 + \mu)I_2 \quad (\text{S18})$$

$$\frac{dR_1}{dt} = \gamma_1 I_1 - \lambda_2 \epsilon_{21} R_1 - \rho_1 R_1 + \rho_2 R - \mu R_1 \quad (\text{S19})$$

$$\frac{dR_2}{dt} = \gamma_2 I_2 - \lambda_1 \epsilon_{12} R_2 - \rho_2 R_2 + \rho_1 R - \mu R_2 \quad (\text{S20})$$

$$\frac{dJ_1}{dt} = \lambda_1 \epsilon_{12} R_2 - (\gamma_1 + \mu)J_1 \quad (\text{S21})$$

$$\frac{dJ_2}{dt} = \lambda_2 \epsilon_{21} R_1 - (\gamma_2 + \mu)J_2 \quad (\text{S22})$$

$$\frac{dR}{dt} = \gamma_1 J_1 + \gamma_2 J_2 - \rho_1 R - \rho_2 R - \mu R \quad (\text{S23})$$

522 where S represents the proportion of individuals who are fully susceptible to infections
 523 by both strains; I_1 represents the proportion of individuals who are infected with strain 1 without prior immunity; I_2 represents the proportion of individuals who are infected with strain 2 without prior immunity; R_1 represents the proportion of individuals who are fully immune against strain 1 and partially susceptible to reinfection by strain 2; R_2 represents the proportion of individuals who are fully immune against strain 2 and partially susceptible to reinfection by strain 1; J_1 represents the proportion of individuals who are infected with strain 1 with prior immunity against strain 2; J_2 represents the proportion of individuals who are infected with strain 2 with prior immunity against strain 1; R represents the proportion of individuals who are immune to infections from both strains; μ represents the birth/death rate; λ_1 and λ_2 represent the force of infection from strains 1 and 2, respectively; ρ_1 and ρ_2 represent the waning immunity rate; γ_1 and γ_2 represent the recovery rate; ϵ_{21} and ϵ_{12} represent the susceptibility to reinfection with strains 2 and 1, respectively, given prior immunity from infection with strains 1 and 2, respectively. The force of infection is modeled as follows:

$$\beta_1 = b_1(1 + \theta_1 \sin(2\pi(t - \phi_1)))\alpha(t) \quad (\text{S24})$$

$$\beta_2 = b_2(1 + \theta_2 \sin(2\pi(t - \phi_2)))\alpha(t) \quad (\text{S25})$$

$$\lambda_1 = \beta_1(I_1 + J_1) \quad (\text{S26})$$

$$\lambda_2 = \beta_2(I_2 + J_2) \quad (\text{S27})$$

538 In Supplementary Figures S2–S4, we assume the following parameters: $b_1 = 2 \times$
 539 $52/\text{years}$, $b_2 = 4 \times 52/\text{years}$, $\phi_1 = \phi_2 = 0$, $\epsilon_{12} = 0.9$, $\epsilon_{21} = 0.5$, $\gamma_1 = \gamma_2 = 52/\text{years}$,
 540 $\rho_1 = \rho_2 = 1/\text{years}$, and $\mu = 1/70/\text{years}$. For all simulations, we assume a 50%
 541 transmission reduction for 6 months from 2020:

$$\alpha(t) = \begin{cases} 0.5 & 2020 \leq t < 2020.5 \\ 1 & \text{otherwise} \end{cases} \quad (\text{S28})$$

542 The seasonal amplitude θ is varied from 0 to 0.4. All simulations were ran from 1900
 543 to 2030 with following initial conditions: $S(0) = 1 - 2 \times 10^{-6}$, $I_1(0) = 1 \times 10^{-6}$,
 544 $I_2(0) = 1 \times 10^{-6}$, $R_1(0) = 0$, $R_2(0) = 0$, $J_1(0) = 0$, $J_2(0) = 0$, and $R(0) = 0$.

545 We consider three scenarios for measuring pathogen resilience: (1) we only have
 546 information about strain 1, (2) we only have information about strain 2, and (3)
 547 we are unable to distinguish between strains. In the first two scenarios (see panels
 548 A–C for strain 1 and panels D–F for strain 2), we consider the dynamics of average
 549 susceptibility for each strain and total prevalence:

$$\bar{S}_1 = S + \epsilon_{12}R_2 \quad (\text{S29})$$

$$\hat{I}_1 = I_1 + J_1 \quad (\text{S30})$$

$$\bar{S}_2 = S + \epsilon_{21}R_1 \quad (\text{S31})$$

$$\hat{I}_2 = I_2 + J_2 \quad (\text{S32})$$

550 In the third scenario (panels G–I), we consider the dynamics of total susceptible and
 551 infected populations:

$$\hat{S} = S + R_2 + R_1 \quad (\text{S33})$$

$$\hat{I} = I_1 + J_1 + I_2 + J_2 \quad (\text{S34})$$

552 These quantities are used to compute the normalized distance from the attractor, as
 553 described in the main text.

554 Estimating intrinsic resilience using mechanistic model

555 We tested whether we can reliably estimate the intrinsic resilience of a system by fit-
 556 ting a mechanistic model. Specifically, we simulated case time series from stochastic
 557 SIRS and two-strain models and fitted a simple, deterministic SIRS model using a
 558 Bayesian framework.

559 We simulated the models in discrete time, incorporating demographic stochastic-
 560 ity:

$$\beta(t) = \mathcal{R}_0 \left(1 + \theta \cos \left(\frac{2\pi t}{364} \right) \right) \alpha(t)(1 - \exp(-\gamma)) \quad (\text{S35})$$

$$\text{FOI}(t) = \beta(t)I(t - \Delta t)/N \quad (\text{S36})$$

$$B(t) \sim \text{Poisson}(\mu N) \quad (\text{S37})$$

$$\Delta S(t) \sim \text{Binom}(S(t - \Delta t), 1 - \exp(-(\text{FOI}(t) + \mu)\Delta t)) \quad (\text{S38})$$

$$N_{SI}(t) \sim \text{Binom}\left(\Delta S(t), \frac{\text{FOI}(t)}{\text{FOI}(t) + \mu}\right) \quad (\text{S39})$$

$$\Delta I(t) \sim \text{Binom}(I(t - \Delta t), 1 - \exp(-(\gamma + \mu)\Delta t)) \quad (\text{S40})$$

$$N_{IR}(t) \sim \text{Binom}\left(\Delta I(t), \frac{\gamma}{\gamma + \mu}\right) \quad (\text{S41})$$

$$\Delta R(t) \sim \text{Binom}(R(t - \Delta t), 1 - \exp(-(\delta + \mu)\Delta t)) \quad (\text{S42})$$

$$N_{RS}(t) \sim \text{Binom}\left(\Delta R(t), \frac{\delta}{\delta + \mu}\right) \quad (\text{S43})$$

$$S(t) = S(t - \Delta t) + N_{RS}(t) + B(t) - \Delta S(t) \quad (\text{S44})$$

$$I(t) = I(t - \Delta t) + N_{SI}(t) - \Delta I(t) \quad (\text{S45})$$

$$R(t) = R(t - \Delta t) + N_{IR}(t) - \Delta R(t) \quad (\text{S46})$$

561 where FOI represent the force of infection; N_{ij} represent the number of individuals
 562 moving from compartment i to j on a given day; and $B(t)$ represents the number
 563 of new births. We simulate the model on a daily scale—assuming 364 days in a
 564 year so that it can be evenly grouped into 52 weeks—with the following parameters:
 565 $\mathcal{R}_0 = 3$, $\theta = 0.1$, $\gamma = 1/7/\text{days}$, $\delta = 1/(364 \times 2)/\text{days}$, $\mu = 1/(364 \times 50)/\text{days}$, and
 566 $N = 1 \times 10^8$. The model is simulated from 1900 to 2030 assuming $S(0) = N/3$,

⁵⁶⁷ $I(0) = 100$, and $R(0) = N - S(0) - I(0)$. The observed incidence from the model is
⁵⁶⁸ then simulated as follows:

$$C(t) = \text{Beta} - \text{Binom}(N_{SI}(t), \rho, k), \quad (\text{S47})$$

⁵⁶⁹ where ρ represents the reporting probability and k represents the overdispersion pa-
⁵⁷⁰ rameter of beta-binomial distribution. We assume $\rho = 0.002$ (i.e., 0.2% probability)
⁵⁷¹ and $k = 1000$.

⁵⁷² We used an analogous approach for the two-strain model:

$$\beta_1(t) = b_1 \left(1 + \theta_1 \cos \left(\frac{2\pi(t - \phi_1)}{364} \right) \right) \alpha(t) \quad (\text{S48})$$

$$\beta_2(t) = b_2 \left(1 + \theta_2 \cos \left(\frac{2\pi(t - \phi_2)}{364} \right) \right) \alpha(t) \quad (\text{S49})$$

$$\text{FOI}_1(t) = \beta_1(t)(I_1(t - \Delta t) + J_1(t - \Delta t))/N \quad (\text{S50})$$

$$\text{FOI}_2(t) = \beta_2(t)(I_2(t - \Delta t) + J_2(t - \Delta t))/N \quad (\text{S51})$$

$$B(t) \sim \text{Poisson}(\mu N) \quad (\text{S52})$$

$$\Delta S(t) \sim \text{Binom}(S(t - \Delta t), 1 - \exp(-(\text{FOI}_1(t) + \text{FOI}_2(t) + \mu)\Delta t)) \quad (\text{S53})$$

$$N_{SI_1}(t) \sim \text{Binom} \left(\Delta S(t), \frac{\text{FOI}_1(t)}{\text{FOI}_1(t) + \text{FOI}_2(t) + \mu} \right) \quad (\text{S54})$$

$$N_{SI_2}(t) \sim \text{Binom} \left(\Delta S(t), \frac{\text{FOI}_2(t)}{\text{FOI}_1(t) + \text{FOI}_2(t) + \mu} \right) \quad (\text{S55})$$

$$\Delta I_1(t) \sim \text{Binom}(I_1(t - \Delta t), 1 - \exp(-(\gamma_1 + \mu)\Delta t)) \quad (\text{S56})$$

$$N_{I_1 R_1}(t) \sim \text{Binom} \left(\Delta I_1(t), \frac{\gamma_1}{\gamma_1 + \mu} \right) \quad (\text{S57})$$

$$\Delta I_2(t) \sim \text{Binom}(I_2(t - \Delta t), 1 - \exp(-(\gamma_2 + \mu)\Delta t)) \quad (\text{S58})$$

$$N_{I_2 R_2}(t) \sim \text{Binom} \left(\Delta I_2(t), \frac{\gamma_2}{\gamma_2 + \mu} \right) \quad (\text{S59})$$

$$\Delta R_1(t) \sim \text{Binom}(R_1(t - \Delta t), 1 - \exp(-(\epsilon_{21}\text{FOI}_2(t) + \rho_1 + \mu)\Delta t)) \quad (\text{S60})$$

$$N_{R_1 S}(t) \sim \text{Binom} \left(\Delta R_1(t), \frac{\rho_1}{\epsilon_{21}\text{FOI}_2(t) + \rho_1 + \mu} \right) \quad (\text{S61})$$

$$N_{R_1 J_2}(t) \sim \text{Binom} \left(\Delta R_1(t), \frac{\epsilon_{21}\text{FOI}_2(t)}{\epsilon_{21}\text{FOI}_2(t) + \rho_1 + \mu} \right) \quad (\text{S62})$$

$$\Delta R_2(t) \sim \text{Binom}(R_2(t - \Delta t), 1 - \exp(-(\epsilon_{12}\text{FOI}_1(t) + \rho_2 + \mu)\Delta t)) \quad (\text{S63})$$

$$N_{R_2 S}(t) \sim \text{Binom} \left(\Delta R_2(t), \frac{\rho_2}{\epsilon_{12}\text{FOI}_1(t) + \rho_2 + \mu} \right) \quad (\text{S64})$$

$$N_{R_2 J_1}(t) \sim \text{Binom} \left(\Delta R_2(t), \frac{\epsilon_{12}\text{FOI}_1(t)}{\epsilon_{12}\text{FOI}_1(t) + \rho_2 + \mu} \right) \quad (\text{S65})$$

$$\Delta J_1(t) \sim \text{Binom}(J_1(t - \Delta t), 1 - \exp(-(\gamma_1 + \mu)\Delta t)) \quad (\text{S66})$$

$$N_{J_1R}(t) \sim \text{Binom}\left(\Delta J_1(t), \frac{\gamma_1}{\gamma_1 + \mu}\right) \quad (\text{S67})$$

$$\Delta J_2(t) \sim \text{Binom}(J_2(t - \Delta t), 1 - \exp(-(\gamma_2 + \mu)\Delta t)) \quad (\text{S68})$$

$$N_{J_2R}(t) \sim \text{Binom}\left(\Delta J_2(t), \frac{\gamma_2}{\gamma_2 + \mu}\right) \quad (\text{S69})$$

$$\Delta R(t) \sim \text{Binom}(R(t - \Delta t), 1 - \exp(-(\rho_1 + \rho_2 + \mu)\Delta t)) \quad (\text{S70})$$

$$N_{RR_1}(t) \sim \text{Binom}\left(\Delta R(t), \frac{\rho_1}{\rho_1 + \rho_2 + \mu}\right) \quad (\text{S71})$$

$$N_{RR_2}(t) \sim \text{Binom}\left(\Delta R(t), \frac{\rho_2}{\rho_1 + \rho_2 + \mu}\right) \quad (\text{S72})$$

$$S(t) = S(t - \Delta t) - \Delta S(t) + B(t) + N_{R_1S}(t) + N_{R_2S}(t) \quad (\text{S73})$$

$$I_1(t) = I_1(t - \Delta t) - \Delta I_1(t) + N_{SI_1}(t) \quad (\text{S74})$$

$$I_2(t) = I_2(t - \Delta t) - \Delta I_2(t) + N_{SI_2}(t) \quad (\text{S75})$$

$$R_1(t) = R_1(t - \Delta t) - \Delta R_1(t) + N_{I_1R_1}(t) + N_{RR_1}(t) \quad (\text{S76})$$

$$R_2(t) = R_2(t - \Delta t) - \Delta R_2(t) + N_{I_2R_2}(t) + N_{RR_2}(t) \quad (\text{S77})$$

$$J_1(t) = J_1(t - \Delta t) - \Delta J_1(t) + N_{R_2J_1}(t) \quad (\text{S78})$$

$$J_2(t) = J_2(t - \Delta t) - \Delta J_2(t) + N_{R_1J_2}(t) \quad (\text{S79})$$

$$R(t) = R(t - \Delta t) - \Delta R(t) + N_{J_1R}(t) + N_{J_2R}(t) \quad (\text{S80})$$

573 We simulate the model on a daily scale with previously estimated parameters for the
 574 RSV-HMPV interaction [19]: $b_1 = 1.7/\text{weeks}$, $b_2 = 1.95/\text{weeks}$, $\theta_1 = 0.4$, $\theta_2 = 0.3$,
 575 $\phi_1 = 0.005 \times 7/364$, $\phi_2 = 4.99 \times 7/364$, $\epsilon_{12} = 0.92$, $\epsilon_{21} = 0.45$, $\gamma_1 = 1/10/\text{days}$,
 576 $\gamma_2 = 1/10/\text{days}$, $\rho_1 = 1/364/\text{days}$, $\rho_2 = 1/364/\text{days}$, $\mu = 1/(70 \times 364)/\text{days}$, and
 577 $N = 1 \times 10^8$. The model is simulated from 1900 to 2030 assuming $S(0) = N - 200$,
 578 $I_1(0) = 100$, $I_2(0) = 100$, $R_1(0) = 0$, $R_2(0) = 0$, $J_1(0) = 0$, $J_2(0) = 0$, and $R(0) = 0$.
 579 The observed incidence for each strain is then simulated as follows:

$$C_1(t) = \text{Beta} - \text{Binom}(N_{SI_1}(t) + N_{R_2J_1}, \rho, k), \quad (\text{S81})$$

$$C_2(t) = \text{Beta} - \text{Binom}(N_{SI_2}(t) + N_{R_1J_2}, \rho, k), \quad (\text{S82})$$

580 where ρ represents the reporting probability and k represents the overdispersion pa-
 581 rameter of beta-binomial distribution. We assume $\rho = 0.002$ (i.e., 0.2% probability)
 582 and $k = 500$. We also consider the total incidence: $C_{\text{total}}(t) = C_1(t) + C_2(t)$.

583 For both models, we consider a more realistic challenges in intervention effects
 584 $\alpha(t)$ to challenge our ability to estimate the intervention effects. Thus, we assume
 585 a 40% transmission reduction for 3 months from March 2020, followed by a 10%
 586 transmission reduction for 6 months, 20% transmission reduction for 3 months, and

587 a final return to normal levels:

$$\alpha(t) = \begin{cases} 1 & t < 2020.25 \\ 0.6 & 2020.25 \leq t < 2020.5 \\ 0.9 & 2020.5 \leq t < 2021 \\ 0.8 & 2021 \leq t < 2021.25 \\ 1 & 2021.25 \leq t \end{cases}. \quad (\text{S83})$$

588 For all simulations, we truncate the time series from the beginning of 2014 to the
589 end of 2023 and aggregate them into weekly cases.

590 To infer intrinsic resilience from time series, we fit a simple discrete time, deter-
591 ministic SIRS model [4]:

$$\Delta t = 1 \text{ week} \quad (\text{S84})$$

$$\text{FOI}(t) = \beta(t)(I(t - \Delta t) + \omega)/N \quad (\text{S85})$$

$$\Delta S(t) = [1 - \exp(-(\text{FOI}(t) + \mu)\Delta t)] S(t - \Delta t) \quad (\text{S86})$$

$$N_{SI}(t) = \frac{\text{FOI}(t)\Delta S(t)}{\text{FOI}(t) + \mu} \quad (\text{S87})$$

$$\Delta I(t) = [1 - \exp(-(\gamma + \mu)\Delta t)] I(t - \Delta t) \quad (\text{S88})$$

$$N_{IR}(t) = \frac{\gamma \Delta I(t)}{\gamma + \mu} \quad (\text{S89})$$

$$\Delta R(t) = [1 - \exp(-(\nu + \mu)\Delta t)] R(t - \Delta t) \quad (\text{S90})$$

$$N_{RS}(t) = \frac{\nu \Delta R(t)}{\nu + \mu} \quad (\text{S91})$$

$$S(t) = S(t - \Delta t) + \mu S - \Delta S(t) + N_{RS}(t) \quad (\text{S92})$$

$$I(t) = I(t - \Delta t) - \Delta I(t) + N_{SI}(t) \quad (\text{S93})$$

$$R(t) = R(t - \Delta t) - \Delta R(t) + N_{IR}(t) \quad (\text{S94})$$

592 where we include an extra term ω to account for external infections. Although actual
593 simulations do not include any external infections, we found that including this term
594 generally helped with model convergence in previous analyses [4]. The transmission
595 rate is divided into a seasonal term $\beta_{\text{seas}}(t)$ (repeated every year) and intervention
596 term $\alpha(t)$, which are estimated jointly:

$$\beta(t) = \beta_{\text{seas}}(t)\alpha(t), \quad (\text{S95})$$

597 where $\alpha < 1$ corresponds to reduction in transmission due to intervention effects. To
598 constrain the smoothness of $\beta_{\text{seas}}(t)$, we impose cyclic, random-walk priors:

$$\beta_{\text{seas}}(t) \sim \text{Normal}(\beta_{\text{seas}}(t - 1), \sigma) \quad t = 2 \dots 52 \quad (\text{S96})$$

$$\beta_{\text{seas}}(1) \sim \text{Normal}(\beta_{\text{seas}}(52), \sigma) \quad (\text{S97})$$

599 [SWP: I noticed that I forgot to put a prior on σ so need to re-do this but won't
600 change the results.] We fix $\alpha(t) = 1$ for all $t < 2020$ and estimate α assuming a
601 normal prior:

$$\alpha \sim \text{Normal}(1, 0.25). \quad (\text{S98})$$

602 We assume weakly informative priors on ω and ν :

$$\omega \sim \text{Normal}(0, 200) \quad (\text{S99})$$

$$\nu \sim \text{Normal}(104, 26) \quad (\text{S100})$$

603 We assume that the true birth/death rates, population sizes, and recovery rates are
604 known. We note, however, that assuming $\gamma = 1/\text{week}$ actually corresponds to a
605 mean simulated infectious period of 1.6 weeks, which is much longer than the true
606 value; this approximation allows us to test whether we can still robustly estimate the
607 intrinsic resilience given parameter mis-specification. Initial conditions are estimated
608 with following priors:

$$S(0) = Ns(0) \quad (\text{S101})$$

$$I(0) = Ni(0) \quad (\text{S102})$$

$$s(0) \sim \text{Uniform}(0, 1) \quad (\text{S103})$$

$$i(0) \sim \text{Half-Normal}(0, 0.001) \quad (\text{S104})$$

609 Finally, the Observation model is specified as follows:

$$\text{Cases}(t) \sim \text{Negative-Binomial}(\rho N_{SI}(t), \phi) \quad (\text{S105})$$

$$\rho \sim \text{Half-Normal}(0, 0.02) \quad (\text{S106})$$

$$\phi \sim \text{Half-Normal}(0, 10) \quad (\text{S107})$$

610 where ρ represents the reporting probability and ϕ represents the negative binomial
611 overdispersion parameter.

612 The model is fitted to four separate time series: (1) incidence time series from
613 the SIRS model, (2) incidence time series for strain 1 from the two-strain model,
614 (3) incidence time series for strain 2 from the two-strain model, and (4) combined
615 incidence time series for strains 1 and 2 from the two-strain model. The model was
616 fitted using rstan [26, 27]. The resulting posterior distribution was used to calculate
617 the intrinsic resilience of the seasonally unforced system with the same parameters;
618 eigenvalues of the discrete-time SIR model were computed by numerically finding
619 the equilibrium and calculating the Jacobian matrix.

620 **Validations for window-selection criteria**

621 We use stochastic SIRS simulations to validate the window-selection criteria that we
622 use for the linear regression for estimating empirical resilience. For each simulation,
623 we begin by generating a random intervention $\alpha(t)$ from a random set of parameters.

624 First, we draw the duration of intervention τ_{npi} from a uniform distribution between
 625 0.5 and 3.5 years. Then, we draw independent normal variables z_i of length $\lfloor 364\tau_{\text{npi}} \rfloor$
 626 with a standard deviation of 0.02 and take a reverse cumulative sum to obtain a
 627 realistic shape for the intervention:

$$x_n = 1 + \sum_{i=n}^{\lfloor 364\tau_{\text{npi}} \rfloor} z_i, \quad n = 1, \dots, \lfloor 364\tau_{\text{npi}} \rfloor. \quad (\text{S108})$$

628 We repeat this random generation process until less than 10% of x_n exceeds 1. Then,
 629 we set any values that are above 1 or below 0 as 1 and 0, respectively. Then, we
 630 randomly draw the minimum transmission during intervention α_{\min} from a uniform
 631 distribution between 0.5 and 0.7 and scale x_n to have a minimum of α_{\min} :

$$x_{\text{scale},n} = \alpha_{\min} + (1 - \alpha_{\min}) \times \frac{x_n - \min x_n}{1 - \min x_n}. \quad (\text{S109})$$

632 This allows us to simulate a realistically shaped intervention:

$$\alpha(t) = \begin{cases} 1 & t < 2020 \\ x_{\text{scale},364(t-2020)} & 2020 \leq t < 2020 + \tau_{\text{npi}} \\ 1 & \tau_{\text{npi}} \leq t \end{cases}. \quad (\text{S110})$$

633 Given this intervention function, we draw \mathcal{R}_0 from a uniform distribution between 1.5
 634 and 3 and the mean duration of immunity $1/\delta$ from a uniform distribution between
 635 0.5 and 2. Then, we simulate the stochastic SIRS model from $S(0) = 10^8/\mathcal{R}_0$ and
 636 $I(0) = 100$ from 1990 to 2025 and truncate the time series to 2014–2025; if the
 637 epidemic becomes extinct before the end of simulation, we discard that simulation
 638 and start over from the intervention generation step. We then apply the window
 639 selection criteria described in the main text to compute the empirical resilience and
 640 compare it against the intrinsic resilience of the seasonally unforced system. We also
 641 compare this with the naive approach that uses the entire distance-from-attractor
 642 time series, starting from the maximum distance. We repeat this procedure 500
 643 times and quantify the correlation between empirical and intrinsic resilience estimates
 644 across two approaches.

Supplementary Figures

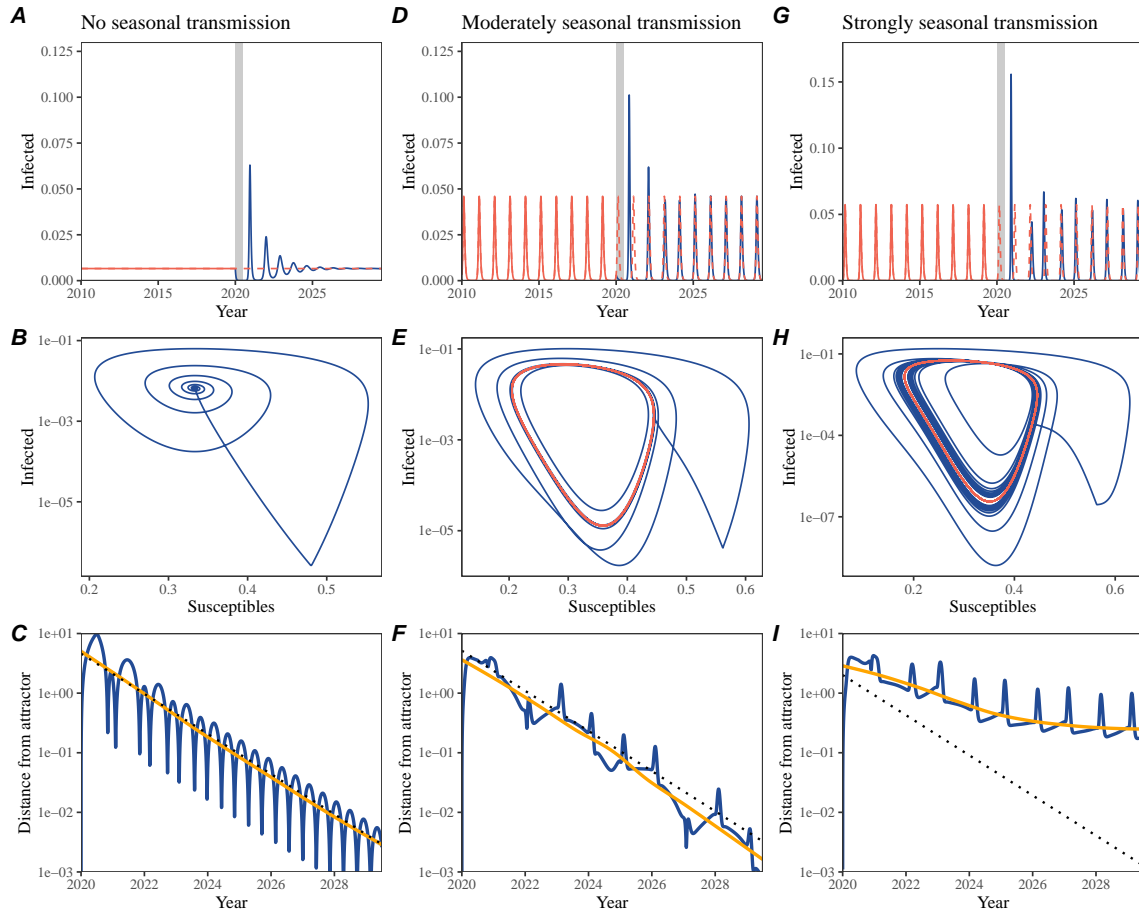


Figure S1: Impact of seasonal transmission on pathogen resilience. (A, D, G) Simulated epidemic trajectories using the SIRS model without seasonal forcing (A), with seasonal forcing of amplitude of 0.2 (D), and with seasonal forcing of amplitude of 0.2 (G). Red and blue solid lines represent epidemic dynamics before and after interventions are introduced, respectively. Red dashed lines represent counterfactual epidemic dynamics in the absence of interventions. Gray regions indicate the duration of interventions. (B, E, H) Phase plane representation of the corresponding model. Red and blue solid lines represent epidemic trajectories on an SI phase plane before and after interventions are introduced, respectively. (C, F, I) Changes in logged distance from attractor over time. Blue lines represent the logged distance from attractor. Orange lines represent the locally estimated scatterplot smoothing (LOESS) fits to the logged distance from attractor. Dotted lines are superimposed as a comparison to have the same slope as the intrinsic resilience of the seasonally unforced system.

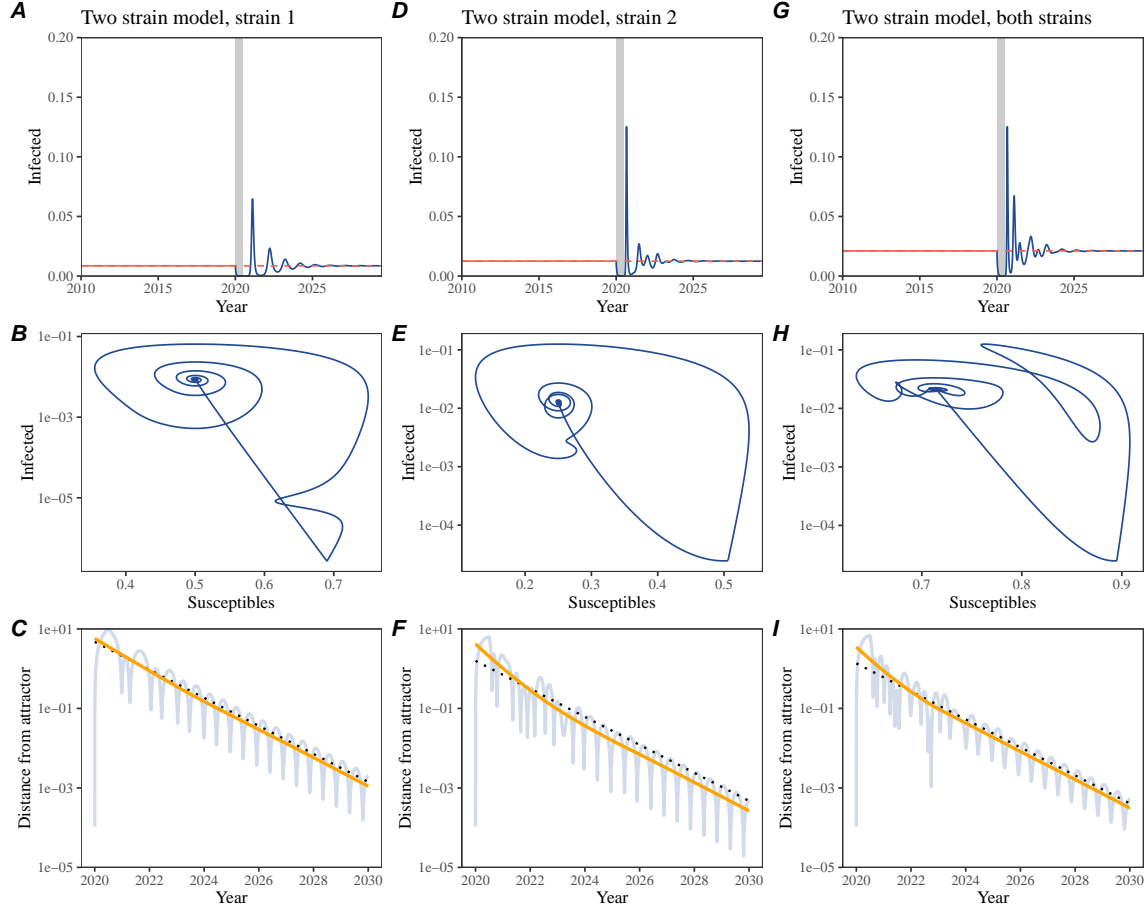


Figure S2: Conceptual framework for measuring pathogen resilience following NPIs for a two-strain system without seasonal forcing. (A, D, G) Simulated epidemic trajectories using a multi-strain system without seasonal forcing. Red and blue solid lines represent epidemic dynamics before and after interventions are introduced, respectively. Red dashed lines represent counterfactual epidemic dynamics in the absence of interventions. Gray regions indicate the duration of interventions. (B, E, H) Phase plane representation of the corresponding model. Red and blue solid lines represent epidemic trajectories on an SI phase plane before and after interventions are introduced, respectively. (C, F, I) Changes in logged distance from attractor over time. Blue lines represent the logged distance from attractor. Orange lines represent the locally estimated scatterplot smoothing (LOESS) fits to the logged distance from attractor. Dotted lines are superimposed as a comparison to have the same slope as the intrinsic resilience of the seasonally unforced system.

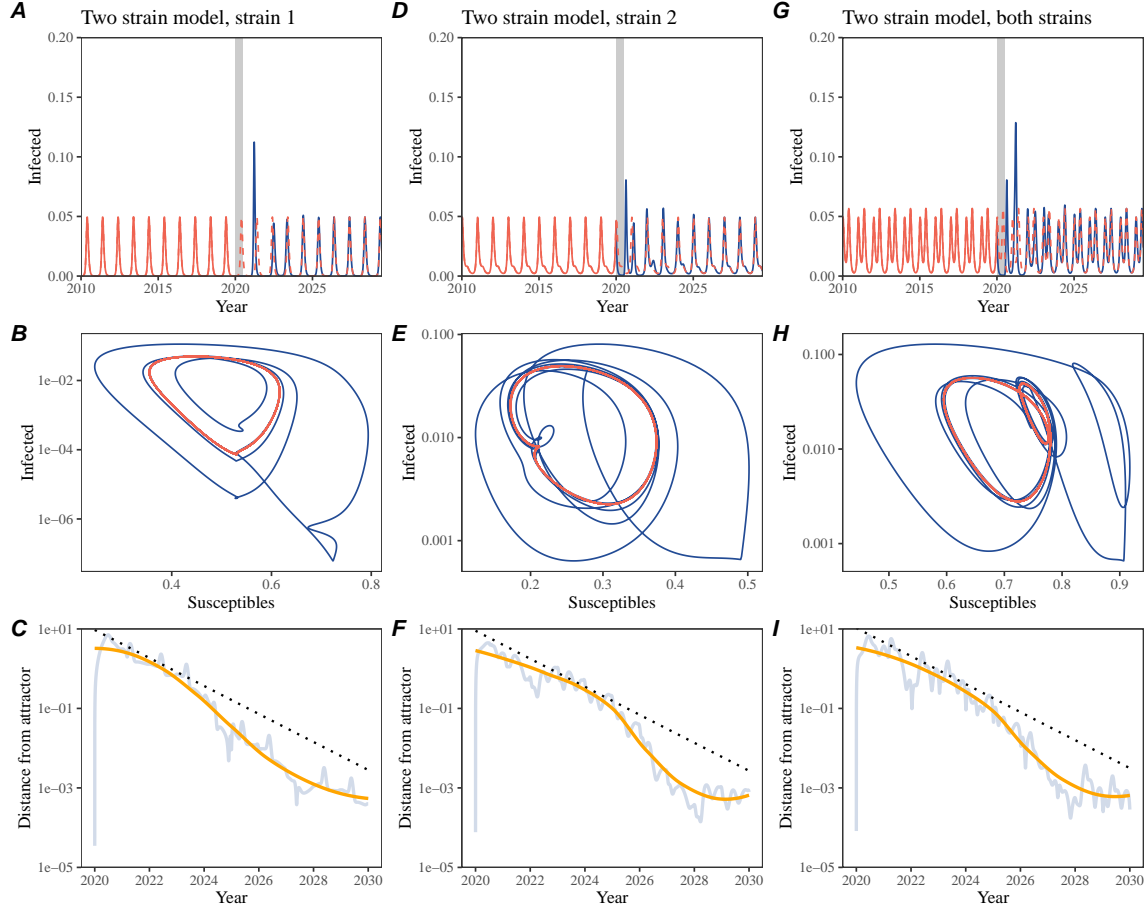


Figure S3: Conceptual framework for measuring pathogen resilience following NPIs for a multi-strain system with seasonal forcing. (A, D, G) Simulated epidemic trajectories using a multi-strain system with seasonal forcing (amplitude of 0.2). Red and blue solid lines represent epidemic dynamics before and after interventions are introduced, respectively. Red dashed lines represent counterfactual epidemic dynamics in the absence of interventions. Gray regions indicate the duration of interventions. (B, E, H) Phase plane representation of the corresponding model. Red and blue solid lines represent epidemic trajectories on an SI phase plane before and after interventions are introduced, respectively. (C, F, I) Changes in logged distance from attractor over time. Blue lines represent the logged distance from attractor. Orange lines represent the locally estimated scatterplot smoothing (LOESS) fits to the logged distance from attractor. Dotted lines are superimposed as a comparison to have the same slope as the intrinsic resilience of the seasonally unforced system.

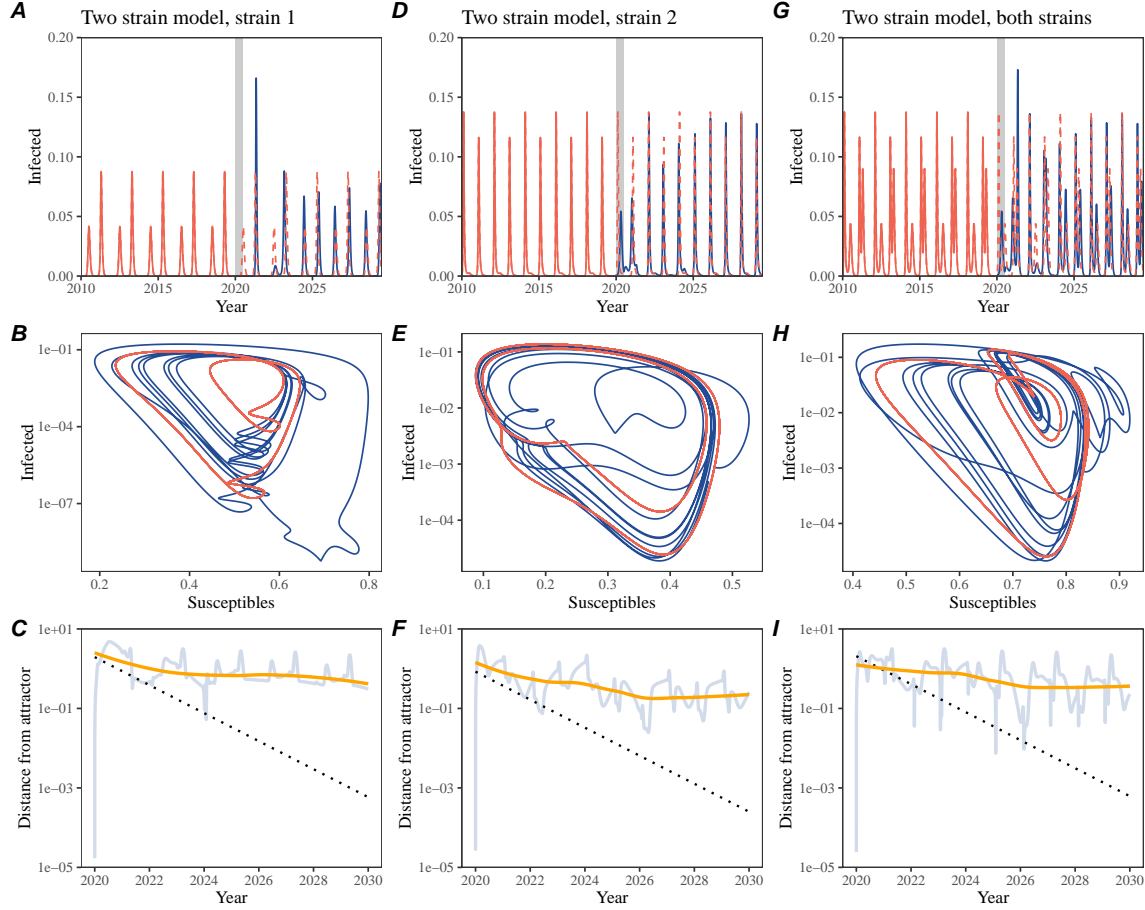


Figure S4: Conceptual framework for measuring pathogen resilience following NPIs for a multi-strain system with strong seasonal forcing. (A, D, G) Simulated epidemic trajectories using a multi-strain system with seasonal forcing (amplitude of 0.4). Red and blue solid lines represent epidemic dynamics before and after interventions are introduced, respectively. Red dashed lines represent counterfactual epidemic dynamics in the absence of interventions. Gray regions indicate the duration of interventions. (B, E, H) Phase plane representation of the corresponding model. Red and blue solid lines represent epidemic trajectories on an SI phase plane before and after interventions are introduced, respectively. (C, F, I) Changes in logged distance from attractor over time. Blue lines represent the logged distance from attractor. Orange lines represent the locally estimated scatterplot smoothing (LOESS) fits to the logged distance from attractor. Dotted lines are superimposed as a comparison to have the same slope as the intrinsic resilience of the seasonally unforced system.

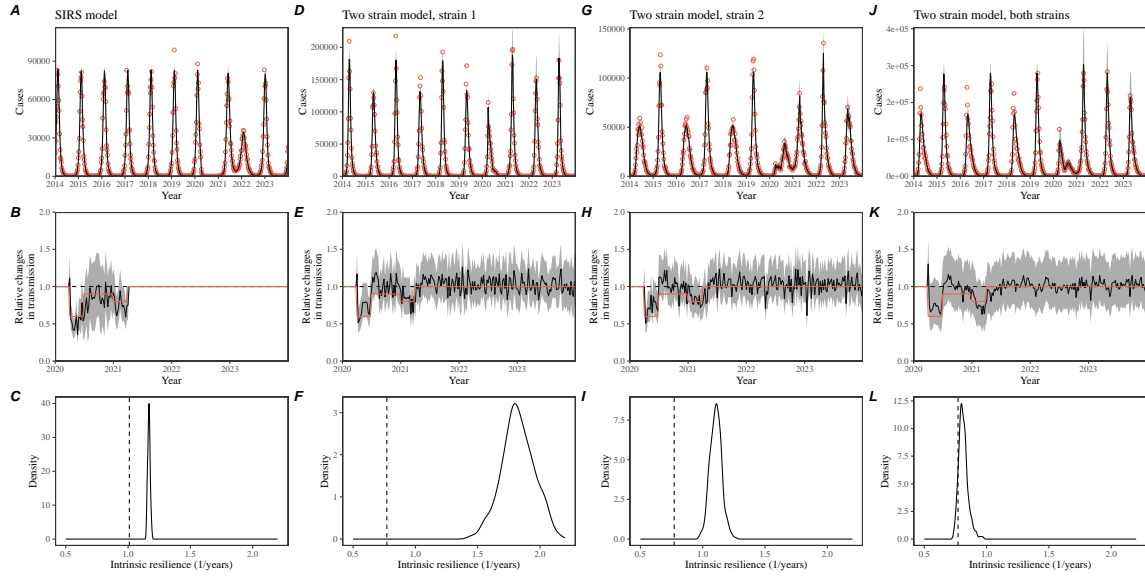


Figure S5: Mechanistic model fits to simulated data and inferred intrinsic resilience. (A, D, G, J) Simulated case time series from corresponding models (red) and SIRS model fits (black). (B, E, H, K) Assumed changes in transmission due to pandemic NPIs (red) and estimated changes from the SIRS model (black). Solid lines and shaded regions represent fitted posterior median and 95% credible intervals. (C, F, I, L) True intrinsic resilience of the seasonally unforced system (vertical lines) and the posterior distribution of the inferred intrinsic resilience from the SIRS model (density plots).

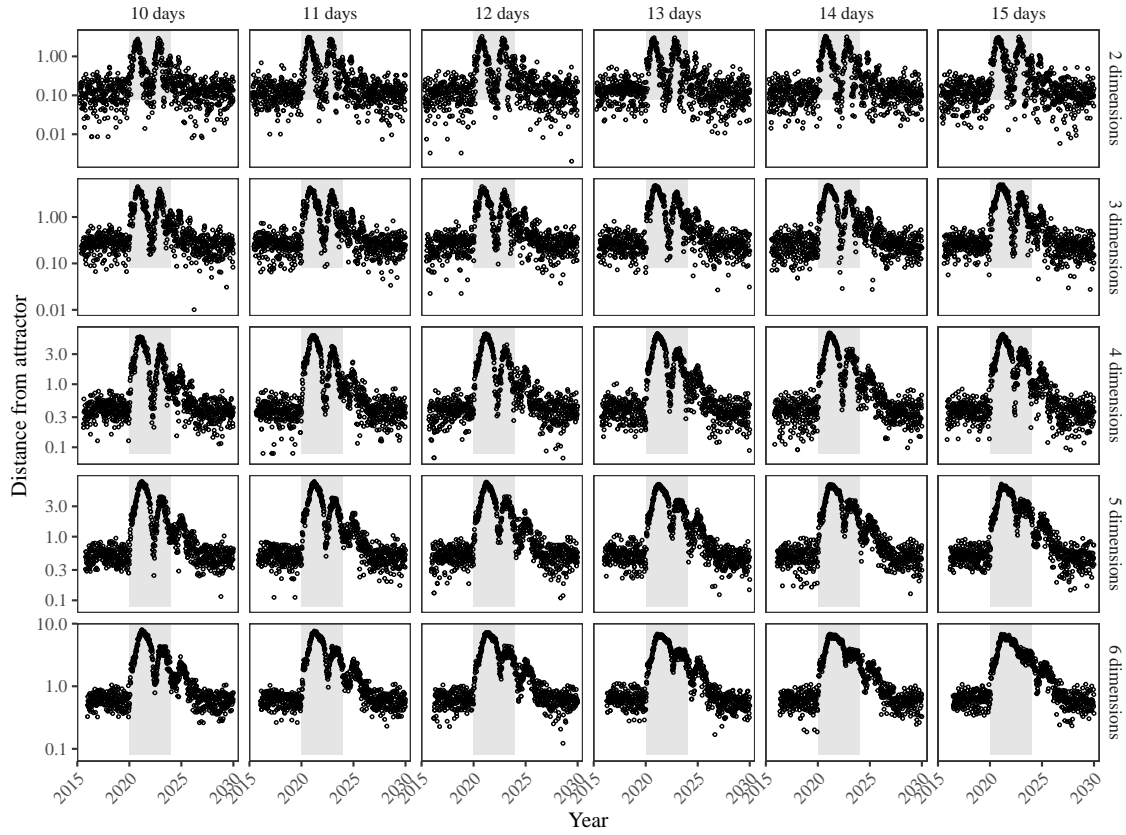


Figure S6: Sensitivity of the distance from attractor to choices about embedding lags and dimensions. Sensitivity analysis for the distance-from-attractor time series shown in Figure 3E in the main text by varying the embedding lag between 10–15 days and embedding dimensions between 2–6 dimensions.

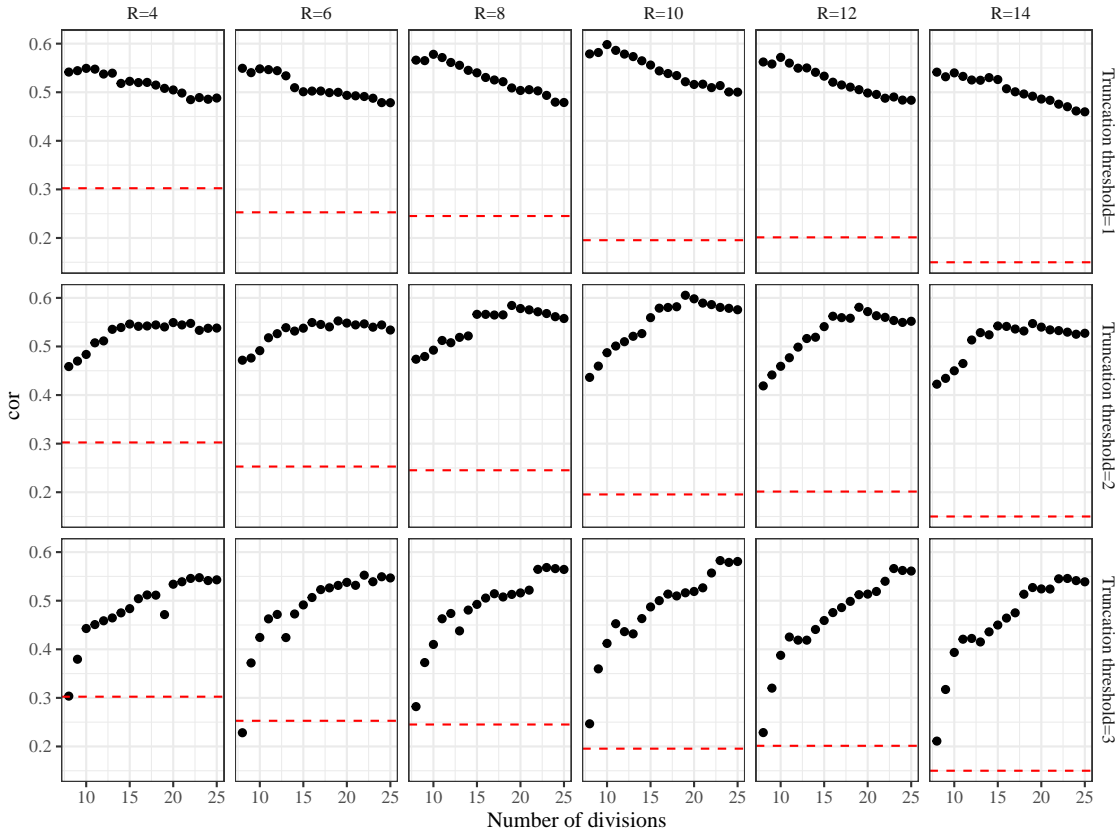


Figure S7: Impact of fitting window selection on the estimation of empirical resilience. We simulated 500 epidemics of a stochastic SIRS model with randomly drawn parameters and randomly generated intervention impacts. For each simulation, we reconstructed the empirical attractor based on the approach outlined in Figure 3 and estimate the distance from attractor. The naive approach fits a linear regression on a log scale, starting from the maximum distance until the end of the time series. The window-based approach tries to select an appropriate window by smoothing the distance estimates and finding the time period when the smoothed time series crosses pre-determined threshold, relative to the maximum distance; then, a linear regression is fitted by using the raw distance within this time period.

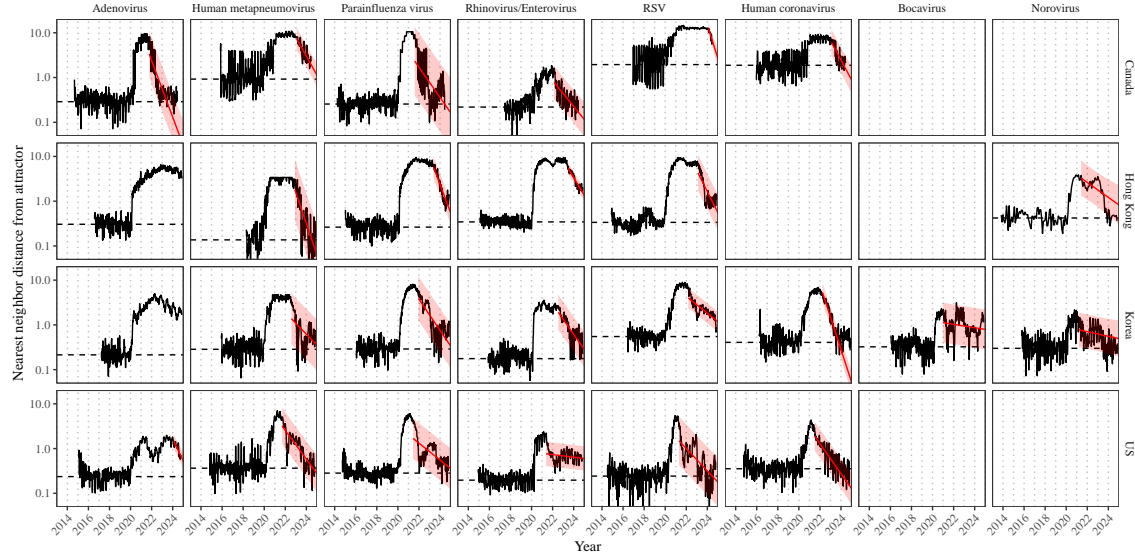


Figure S8: Estimated time series of distance from attractor for each pathogen across Canada, Hong Kong, Korea, and the US. Black lines represent the estimated distance from attractor. Red lines and shaded regions represent the linear regression fits and corresponding 95% confidence intervals. Dashed lines represent the average of the pre-pandemic nearest neighbor distances.

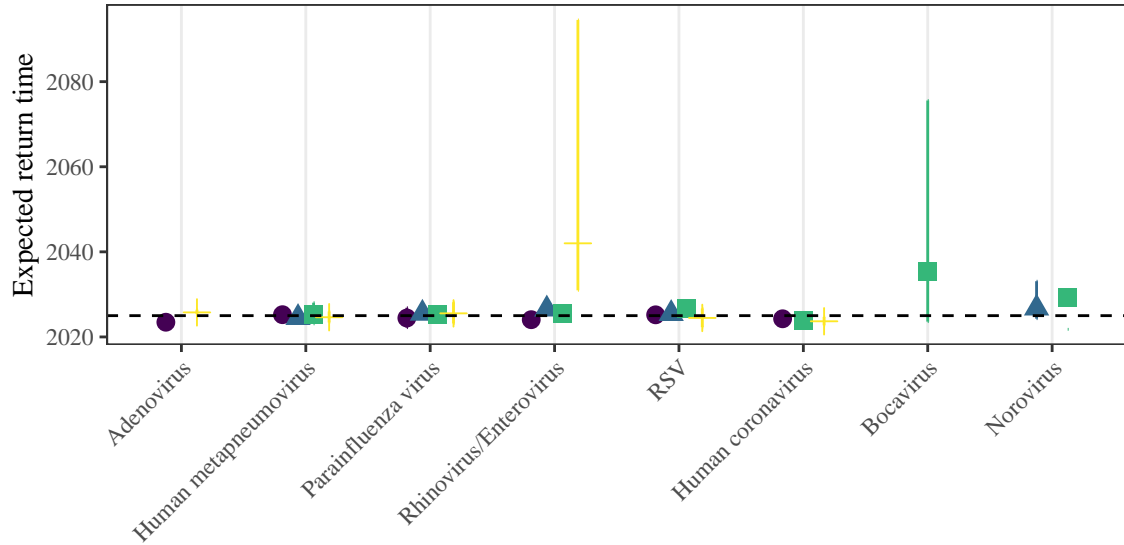


Figure S9: **Predicted timing of when each pathogen will return to their pre-pandemic cycles (zoomed out).** The dashed line in panel B indicates the end of 2024 (current observation time). Error bars represent 95% confidence intervals.

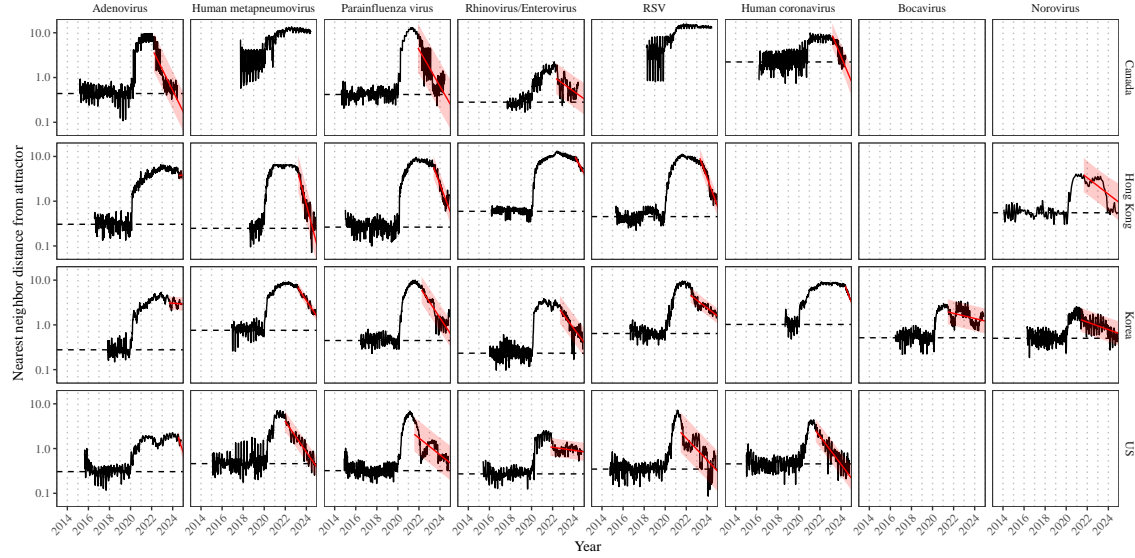


Figure S10: Estimated time series of distances from the attractor for each pathogen across Canada, Hong Kong, Korea, and the US using higher embedding dimensions. Black lines represent the estimated distance from attractor. Red lines and shaded regions represent the linear regression fits and corresponding 95% confidence intervals. Dashed lines represent the average of the pre-pandemic nearest neighbor distances. A lower threshold is used for determining embedding dimensions with the false nearest neighbors approach, thereby yielding a higher embedding dimension.

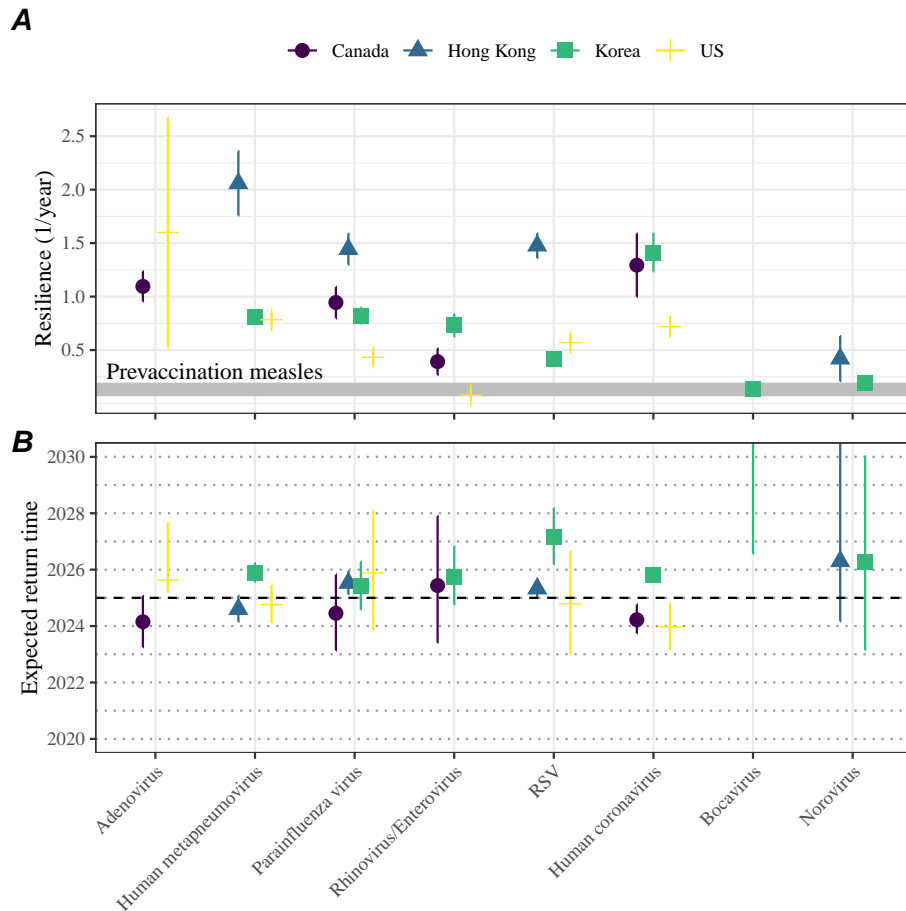


Figure S11: **Summary of resilience estimates using higher embedding dimensions.** (A) Estimated pathogen resilience. The gray horizontal line represents the intrinsic resilience of pre-vaccination measles dynamics. (B) Predicted timing of when each pathogen will return to their pre-pandemic cycles. The dashed line in panel B indicates the end of 2024 (current observation time). Error bars represent 95% confidence intervals. A lower threshold is used for determining embedding dimensions with the false nearest neighbors approach, thereby yielding a higher embedding dimension.

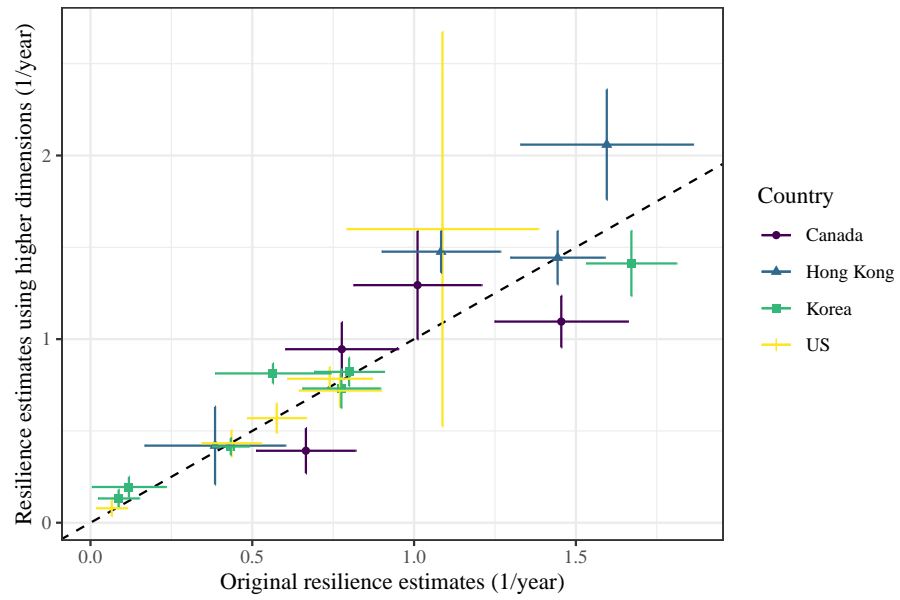


Figure S12: **Comparison of resilience estimates.** Each point represents a resilience estimate for a specific pathogen at a specific country. The x values represent the original resilience estimates presented in Figure 4. The y values represent the original resilience estimates presented in Supplementary Figure S11.

646 **References**

- 647 [1] Rachel E Baker, Sang Woo Park, Wenchang Yang, Gabriel A Vecchi, C Jessica E
648 Metcalf, and Bryan T Grenfell. The impact of COVID-19 nonpharmaceutical
649 interventions on the future dynamics of endemic infections. *Proceedings of the*
650 *National Academy of Sciences*, 117(48):30547–30553, 2020.
- 651 [2] Gabriela B Gomez, Cedric Mahé, and Sandra S Chaves. Uncertain effects of the
652 pandemic on respiratory viruses. *Science*, 372(6546):1043–1044, 2021.
- 653 [3] Mihaly Koltai, Fabienne Krauer, David Hodgson, Edwin van Leeuwen, Marina
654 Treskova-Schwarzbach, Mark Jit, and Stefan Flasche. Determinants of RSV
655 epidemiology following suppression through pandemic contact restrictions. *Epi-*
656 *demics*, 40:100614, 2022.
- 657 [4] Sang Woo Park, Brooklyn Noble, Emily Howerton, Bjarke F Nielsen, Sarah
658 Lentz, Lilliam Ambroggio, Samuel Dominguez, Kevin Messacar, and Bryan T
659 Grenfell. Predicting the impact of non-pharmaceutical interventions against
660 COVID-19 on *Mycoplasma pneumoniae* in the United States. *Epidemics*,
661 49:100808, 2024.
- 662 [5] Amanda C Perofsky, Chelsea L Hansen, Roy Burstein, Shanda Boyle, Robin
663 Prentice, Cooper Marshall, David Reinhart, Ben Capodanno, Melissa Truong,
664 Kristen Schwabe-Fry, et al. Impacts of human mobility on the citywide trans-
665 mission dynamics of 18 respiratory viruses in pre-and post-COVID-19 pandemic
666 years. *Nature communications*, 15(1):4164, 2024.
- 667 [6] Eric J Chow, Timothy M Uyeki, and Helen Y Chu. The effects of the COVID-19
668 pandemic on community respiratory virus activity. *Nature Reviews Microbiol-*
669 *ogy*, 21(3):195–210, 2023.
- 670 [7] Stephen M Kissler, Christine Tedijanto, Edward Goldstein, Yonatan H Grad,
671 and Marc Lipsitch. Projecting the transmission dynamics of SARS-CoV-2
672 through the postpandemic period. *Science*, 368(6493):860–868, 2020.
- 673 [8] Rachel E Baker, Chadi M Saad-Roy, Sang Woo Park, Jeremy Farrar, C Jessica E
674 Metcalf, and Bryan T Grenfell. Long-term benefits of nonpharmaceutical inter-
675 ventions for endemic infections are shaped by respiratory pathogen dynamics.
676 *Proceedings of the National Academy of Sciences*, 119(49):e2208895119, 2022.
- 677 [9] John-Sebastian Eden, Chisha Sikazwe, Ruopeng Xie, Yi-Mo Deng, Sheena G
678 Sullivan, Alice Michie, Avram Levy, Elena Cutmore, Christopher C Blyth,
679 Philip N Britton, et al. Off-season RSV epidemics in Australia after easing
680 of COVID-19 restrictions. *Nature communications*, 13(1):2884, 2022.
- 681 [10] Stuart L Pimm. The structure of food webs. *Theoretical population biology*,
682 16(2):144–158, 1979.

- 683 [11] Michael G Neubert and Hal Caswell. Alternatives to resilience for measuring
684 the responses of ecological systems to perturbations. *Ecology*, 78(3):653–665,
685 1997.
- 686 [12] Lance H Gunderson. Ecological resilience—in theory and application. *Annual
687 review of ecology and systematics*, 31(1):425–439, 2000.
- 688 [13] Vasilis Dakos and Sonia Kéfi. Ecological resilience: what to measure and how.
689 *Environmental Research Letters*, 17(4):043003, 2022.
- 690 [14] Floris Takens. Detecting strange attractors in turbulence. In *Dynamical Sys-
691 tems and Turbulence, Warwick 1980: proceedings of a symposium held at the
692 University of Warwick 1979/80*, pages 366–381. Springer, 2006.
- 693 [15] Jonathan Dushoff, Joshua B Plotkin, Simon A Levin, and David JD Earn. Dynamical resonance can account for seasonality of influenza epidemics. *Pro-
694 ceedings of the National Academy of Sciences*, 101(48):16915–16916, 2004.
- 695 [16] Alan Hastings, Karen C Abbott, Kim Cuddington, Tessa Francis, Gabriel Gell-
696 ner, Ying-Cheng Lai, Andrew Morozov, Sergei Petrovskii, Katherine Scran-
697 ton, and Mary Lou Zeeman. Transient phenomena in ecology. *Science*,
698 361(6406):eaat6412, 2018.
- 699 [17] Matthew B Kennel, Reggie Brown, and Henry DI Abarbanel. Determining
700 embedding dimension for phase-space reconstruction using a geometrical con-
701 struction. *Physical review A*, 45(6):3403, 1992.
- 702 [18] Eugene Tan, Shannon Algar, Débora Corrêa, Michael Small, Thomas Stemler,
703 and David Walker. Selecting embedding delays: An overview of embedding
704 techniques and a new method using persistent homology. *Chaos: An Interdis-
705 ciplinary Journal of Nonlinear Science*, 33(3), 2023.
- 706 [19] Samit Bhattacharyya, Per H Gesteland, Kent Korgenski, Ottar N Bjørnstad,
707 and Frederick R Adler. Cross-immunity between strains explains the dynamical
708 pattern of paramyxoviruses. *Proceedings of the National Academy of Sciences*,
709 112(43):13396–13400, 2015.
- 710 [20] Bryan T Grenfell, Ottar N Bjørnstad, and Bärbel F Finkenstädt. Dynamics of
711 measles epidemics: scaling noise, determinism, and predictability with the TSIR
712 model. *Ecological monographs*, 72(2):185–202, 2002.
- 713 [21] Virginia E Pitzer, Cécile Viboud, Vladimir J Alonso, Tanya Wilcox, C Jessica
714 Metcalf, Claudia A Steiner, Amber K Haynes, and Bryan T Grenfell. Environ-
715 mental drivers of the spatiotemporal dynamics of respiratory syncytial virus in
716 the United States. *PLoS pathogens*, 11(1):e1004591, 2015.
- 717

- 718 [22] Katharine R Dean, Fabienne Krauer, Lars Walløe, Ole Christian Lingjærde, Bar-
719 bara Bramanti, Nils Chr Stenseth, and Boris V Schmid. Human ectoparasites
720 and the spread of plague in Europe during the Second Pandemic. *Proceedings*
721 *of the National Academy of Sciences*, 115(6):1304–1309, 2018.
- 722 [23] Margarita Pons-Salort and Nicholas C Grassly. Serotype-specific immunity
723 explains the incidence of diseases caused by human enteroviruses. *Science*,
724 361(6404):800–803, 2018.
- 725 [24] Sarah Cobey and Edward B Baskerville. Limits to causal inference with state-
726 space reconstruction for infectious disease. *PLoS one*, 11(12):e0169050, 2016.
- 727 [25] Edward Goldstein, Sarah Cobey, Saki Takahashi, Joel C Miller, and Marc Lip-
728 sitch. Predicting the epidemic sizes of influenza A/H1N1, A/H3N2, and B: a
729 statistical method. *PLoS medicine*, 8(7):e1001051, 2011.
- 730 [26] Bob Carpenter, Andrew Gelman, Matthew D Hoffman, Daniel Lee, Ben
731 Goodrich, Michael Betancourt, Marcus A Brubaker, Jiqiang Guo, Peter Li,
732 and Allen Riddell. Stan: A probabilistic programming language. *Journal of*
733 *statistical software*, 76, 2017.
- 734 [27] Stan Development Team. RStan: the R interface to Stan, 2024. R package
735 version 2.32.6.